1-1-2008

Effect of heat treatment on mechanical properties of bio-medical Ti-6A1-4V eli alloy

Balaji Devatha Venkatesh
Ryerson University

EFFECT OF HEAT TREATMENT ON MECHANICAL PROPERTIES OF BIO-MEDICAL Ti-6Al-4V ELI ALLOY

By

Balaji Devatha Venkatesh

B. E., Mechanical Engineering

Bangalore University

Bangalore, India, 1999

A thesis presented to Ryerson University
in partial fulfillment of the
requirements for the degree of
Master of Applied Science
in the Program of
Mechanical Engineering

Toronto, Ontario, Canada, 2008

AUTHOR'S DECLARATION

I hereby declare that I am the sole author of this thesis.

Balaji Devatha Venkatesh:_____

I authorize Ryerson University to lend this thesis to other institutes or other individuals for the purpose of scholarly research.

Balaji Devatha Venkatesh:_____

I further authorize Ryerson University to reproduce this thesis by photocopying or by other means, in total or in part, at the request of other institutions or individuals for the purpose of scholarly research.

Balaji Devatha Venkatesh:_____

BORROWER'S PAGE

Ryerson University requires the signature of all persons using or photocopying this thesis. Please sign below provide address and date.

Name	Address	Date

EFFECT OF HEAT TREATMENT ON MECHANICAL PROPERTIES OF BIO-MEDICAL Ti-6Al-4V ELI ALLOY

Balaji Devatha Venkatesh

M. A. Sc., Mechanical Engineering
Ryerson University, Toronto, 2008

Abstract

Ti-6Al-4V alloy of extra low interstitial (ELI) grade has been used in biomedical applications because of its high strength-to-weight ratio and excellent biocompatibility. However, its poor wear resistance requires proper surface hardening. Body implants are also subjected to loads at varying strain rates. The objective of this study was to change the microstructure of Ti-6Al-4V ELI alloy via heat treatment and evaluate the mechanical properties with or without a hardened surface layer. It was observed that the hardened surface layer had only a small effect on the yield and tensile strengths but reduced ductility. The strain hardening exponent decreased with increasing strain rate. The strain rate sensitivity decreased as the true strain increased. The fractal dimension of fracture surfaces was observed to be associated with the strength and ductility. Fatigue crack initiation was observed to occur at the specimen surface, regardless of the applied strain amplitudes and heat treatment conditions.

ACKNOWLEDGEMENTS

I would like to thank my supervisors Dr. Daolun Chen and Dr. Sanjeev Bhole for their invaluable guidance and support during my M.A.Sc. studies at Ryerson University. I express my deep gratitude for their detailed review, constructive comments and excellent advice during my research period. They were always accessible and willing to help their students with their research. Their scientific rigor and encouragement from different perspectives are highly beneficial not only in my academic life but also in my future professional life.

I am grateful to Natural Sciences and Engineering Research Council (NSERC) of Canada and Premier Research Excellence Award (PREA) for the financial support for this project.

I would like to extend my thanks to all my friends and colleagues at Ryerson University for helping me and keeping my spirits up. Special thanks are owed to A. Machin, Q. Li, J. Amankrah, D. Ostrom and R. Churaman for their strong support to easy access to the lab facilities.

I would like to express my deepest gratitude to my loving parents and my sister, for their persistent encouragement and emotional support. Last but not least for my relatives and friends. A very special thanks to my dearest friend who is fighting for her life, for her constant support and encouragement.

TABLE OF CONTENTS

Author's Declaration..... ii

Borrower's page.....iii

Abstract.....iv

Acknowledgements..... v

Table of contents..... vi

List of Tables..... ix

List of Figures..... x

Nomenclature.....xvi

Chapter 1 Introduction..... 1

Chapter 2 Literature Review.....5

2.1 Microstructure..... 5

2.2 Hardness..... 9

2.3 Tensile and fatigue data.....13

Chapter 3 Material and Experimental Procedure.....20

3.1 Material and heat treatment.....20

3.2 Microstructure and hardness tests.....22

3.3 Tensile and fatigue tests..... 22

3.4 Fractography and fractal analysis.....23

Chapter 4 Tensile Properties.....25

4.1 Microstructure and microhardness..... 25

4.2 Effect of heat treatment on the tensile properties..... 28

4.3 Strain hardening behavior..... 34

4.4 Strain rate sensitivity.....38

Chapter 5 Low Cycle Fatigue Properties.....42

5.1 Stress amplitude..... 42

5.2 Hysteresis loops and mean stress change.....44

5.3 Fatigue life.....48

Chapter 6 Fractals and Fractography.....51

6.1 Introduction to fractal analysis in materials science.....51

6.1.1 Contradictory relationships..... 52

6.1.2 Methods of measuring fractals..... 53

6.2 Three-dimensional fractal measurement 54

6.3 Variation of strength, ductility and roughness with the fractal dimension.....56

6.4 Examination of fatigue fracture surfaces 60

Chapter 7 Conclusions and Future Work.....64

7.1 Conclusions 64

7.2 Recommendations for future work.....67

Chapter 8 References.....68

LIST OF TABLES

Table 2.1 Mechanical properties of titanium alloys for biomedical applications [10]... 13

Table 2.2 Tensile properties of Ti–6Al–4V seamless tubes [35] 14

Table 2.3 Fatigue properties of Ti–6Al–4V seamless tubes [35]..... 14

Table 3.1 Chemical composition of as-received Ti-6Al-4V ELI (weight percent).....20

Table 4.1 Strain-rate sensitivity values for the air cooling (AC) specimens, evaluated via the common approach (m) and Lindholm approach (m_L).....40

LIST OF FIGURES

Figure 1.1 The hip and knee implants from Biomet.com [12]..... 2

Figure 1.2 Fatigue fracture in an implant of (a) 27 year old woman weighing 74 kg (b) 76 year old woman weighing 71 kg [16]..... 3

Figure 2.1 Ti-6Al-4V quenched from the β field, etched with benzol chloride + HF (hydrogen fluoride) [30]..... 7

Figure 2.2 Ti-6Al-4V alloy furnace cooled from the β field into the α+β field at 930 °C, held 46 h, water quenched, reheated to 770°C and again water quenched [30]..... 7

Figure 2.3 Ti-6Al-4V alloy held at 930 °C for 72 h and water-quenched, reheated at 740 °C for 2 h and quenched [30]..... 8

Figure 2.4 Ti-6Al-4V held at 910 °C for 20 h, furnace cooled to 790 °C, held 1 h and quenched [30]..... 8

Figure 2.5 Hardness profiles of Ti6Al4V treated by plasma immersion ion implantation at 800°C, for different treatment times [32]..... 10

Figure 2.6 Microhardness profiles (VHN 0.02) on cross-sections of specimens subjected to different treatments in the glow discharge plasma; in the inset, the surface microhardness (VHN 0.10) of the specimens is given as well [33]..... 11

Figure 2.7 hardness-depth profile of the sample oxidized for 60 h (ODZ: oxygen diffusion zone; BM: base metal) [29]..... 12

Figure 2.8 Relationship between residual tensile strength or 0.2% proof stress after fatigue, as a function of number of cycles [15].....16

Figure 2.9 Flow stress versus strain behavior of ELI grade Ti-6Al-4V at 750 °C at various strain rates [3]..... . 17

Figure 2.10 Flow stress versus strain behavior of ELI grade Ti-6Al-4V at 950 °C at various strain rates [3]..... 17

Figure 2.11 Flow stress versus strain behavior of ELI grade Ti-6Al-4V at 1050 °C at various strain rates [3]..... 18

Figure 2.12 The strain rate sensitivity index m at various temperatures and key strain rates [3]..... . 19

Figure 3.1 Geometry and dimensions of the tensile and fatigue specimens used in the present study.....20

Figure 3.2 Typical phase diagram of Ti-6Al-4V alloy..... 21

Figure 3.3 Schematic illustration of heat treatment procedure.....22

Figure 3.4 Picture of Instron 8801 servo-hydraulic testing system.....23

Figure 3.5 Picture of Scanning electron microscope (SEM) coupled with energy dispersive X-ray spectroscopy.....24

Figure 4.1 Microstructures of Ti-6Al-4V ELI alloy in different conditions, (a) as-received, (b) water quenching (WQ), (c) air cooling (AC), (d) furnace cooling (FC) (e) AC +aging and (f) WQ + aging..... 26

Figure 4.2 Knoop microhardness profile of the Ti-6Al-4V ELI alloy in all conditions..... 28

Figure 4.3 Stress-strain curves in the AC + aging condition with and without pickling tested at a strain rate of 1×10^{-4} s^{-1} 29

Figure 4.4 Stress- strain curves versus the strain rates in the AC + aging condition.....30

Figure 4.5 Stress-strain curves of Ti-6Al-4V ELI alloy in different heat treatment conditions tested at a strain rate of 1×10^{-3} s^{-1}.....31

Figure 4.6 Effect of strain rate on the yield strength of Ti-6Al-4V ELI alloy in different heat treatment conditions..... 32

Figure 4.7 Effect of strain rate on the ultimate tensile strength of Ti-6Al-4V ELI alloy in different heat treatment conditions.....33

Figure 4.8 Effect of strain rate on the ductility of Ti-6Al-4V ELI alloy in different heat treatment conditions.....34

Figure 4.9 Strain hardening exponent *n* evaluated on the basis of Hollomon equation as a function of strain rate in the different conditions.....35

Figure 4.10 Strain hardening exponent n_1 evaluated on the basis of Ludwig equation as a function of strain rate in the different conditions.....36

Figure 4.11 Strain hardening exponent n* as a function of strain rates in the different conditions.....37

Figure 4.12 Strain hardening rate versus true stress for the Ti-6Al-4V ELI alloy in different conditions tested at a strain rate of 0.0001 s^{-1}.....39

Figure 4.13 A typical plot of ln(true stress) versus ln(strain rate) to evaluate the strain rate sensitivity, *m*, at different true strain values using the common approach for the AC+aging specimens.....40

Figure 4.14 A typical plot of true stress versus log(strain rate) to determine the strain rate sensitivity, m_L, at different true strain values using the Lindholm approach for the AC+aging specimens.....41

Figure 5.1 Stress amplitude as a function of the number of cycles at different total strain amplitudes for the AC condition.....43

Figure 5.2 Stress amplitude as a function of the number of cycles at a strain amplitude of 0.4% for three material conditions.....43

Figure 5.3 Typical stress-strain hysteresis loops of AC sample at the half-life at a total strain amplitude of 0.4%, 0.6% and 0.8%.....44

Figure 5.4 Typical stress-strain hysteresis loops of different cycles for the AC sample at a total strain amplitude of 0.4%.....45

Figure 5.5 Typical stress-strain hysteresis loops of different cycles for the AC sample at a total strain amplitude of 0.8%.....46

Figure 5.6 Variation of mean stress with the number of cycles at different total strain amplitudes for the AC material.....47

Figure 5.7 Variation of mean stress with the number of cycles at a strain amplitude of 0.4% for three material conditions.....48

Figure 5.8 Effect of the total strain amplitude on fatigue lifetime of the Ti-6Al-4V ELI alloy in the three material conditions.....49

Figure 6.1 A typical plot of the relative area versus the lateral resolution (ruler scale) in a double-log coordinate for the specimen subjected to heat treatment at 955°C and air cooling.....55

Figure 6.2 Variation of yield strength and ultimate tensile strength, with fractal dimension of fracture surfaces in Ti-6Al-4V ELI alloy.....56

Figure 6.3 Variation of ductility, with fractal dimension of fracture surfaces in Ti-6Al-4V ELI alloy.....57

Figure 6.4 Average roughness S_a versus fractal dimension of fracture surfaces in Ti-6Al-4V ELI alloy.....58

Figure 6.5 SEM micrographs of the test specimens in different conditions, (a) as-received, (b) furnace cooling, (c) air cooling, (d) air cooling plus aging, (e) water quenching and (f) water quenching plus aging.....61

Figure 6.6 Typical SEM micrographs of the Ti-6Al-4V ELI alloy in the AC condition after low cycle fatigue tests. (a) low-magnification SEM images showing the overall view of the fracture surface at a total strain amplitude of 0.4%, (b) low-magnification SEM images showing the overall view of the fracture surface at a total strain amplitude of 0.8%, (c) SEM image showing the overall view of the fracture surface at a total strain amplitude of 0.4% for another AC sample at a higher magnification, (d) SEM image at higher magnification showing the crack propagation zone.....62

Figure 6.7 Typical SEM micrographs of the Ti-6Al-4V ELI alloy in the FC condition fatigued at a total strain amplitude of 0.4%. (a) low-magnification SEM image showing the crack initiation site at the specimen surface. (b) SEM image at a higher magnification showing the crack initiation area near the specimen surface, (c) SEM image showing the crack propagation area close to the initiation site. (d) SEM image showing the crack propagation zone at a higher magnification.....63

NOMENCLATURE

Acronym	Definition
3D	three-dimensional
AC	air cooling
ASTM	American Society for Testing and Materials
BCC	body center cubic
BM	base metal
CNC	computer numerical control
CFH	cubic feet per hour
DEM	digital elevation model
EDS	energy dispersive X-ray spectroscopy
ELI	extra low interstitial
FC	furnace cooling
HCP	hexagonal close packing
LCF	low cycle fatigue
ODZ	oxygen diffusion zone
SEM	Scanning electron microscope
UTS	ultimate tensile strength
VHN	Vickers hardness number
WQ	water quenching
YS	yield strength

Symbol	Definition
A_e	evaluation area
b	slope of n versus $\lg \dot{\varepsilon}$
C	a constant
D_f	fractal dimension
K	strength coefficient according to Hollomon equation
K_1	strength coefficient as per Ludwig equation
K^*	strength coefficient as per modified equation
m	strain-rate sensitivity based on common approach
m_L	strain-rate sensitivity based on Lindholm approach
N	number of cycles
N_f	number of cycles to failure
n	strain hardening exponent according to Hollomon equation
n_0	material constant
n_1	strain hardening exponent as per Ludwig equation
n^*	strain hardening exponent as per modified equation
R_0	a constant
R_s	measured relative area
r	linear scale (i.e., side length of equilateral triangles in μm or nm)
S_a	average surface roughness
$Z(x,y)$	height function representing point by point deviations between the measured topography and the mean surface.

ε	true strain
$\dot{\varepsilon}$	true strain-rate
σ	true stress
σ_y	yield strength

CHAPTER ONE

Introduction

It has been reported that nearly 19,500 of previous hip replacements (or about 12.8% of the 152,000 total hip replacements performed in 2000) involved painful revision surgeries, and the number of the total hip replacements is estimated to reach about 272,000 annually by 2030 in the US alone. As the life expectancy of the patient increases, such a high worrisome percentage would further increases, since the life expectancy of the current implant (with normal implant longevity of 12 to 15 years) cannot meet the ever-increasing life expectancy of the patient [1]. These data and predictions highlight an ever-increasing need for materials specifically suited for biomedical applications with improved long-term performance. The implant materials used in orthopedic surgery should not only avoid short-term rejection and infection, but also provide long-term biocompatibility and durability (i.e., high strength, long lifetime, high-wear resistance, high resistance to corrosion in the human body environment, no toxicity to human body, etc.) [2].

Ti-based alloys have excellent biocompatibility, low density, relatively low elastic modulus and excellent corrosion resistance [2-10]. Thus, they have become very good candidates as implant materials. The commonly-used Ti-based implant materials in orthopedic surgery are pure Ti and Ti-6Al-4V [2,8-11]. Current uses of Ti-6Al-4V ELI (extra low interstitial) alloy include hip and knee joints prosthesis, trauma/fixation

devices and dental implants [1,3]. Typical hip and knee implants used are shown in figure 1.1.

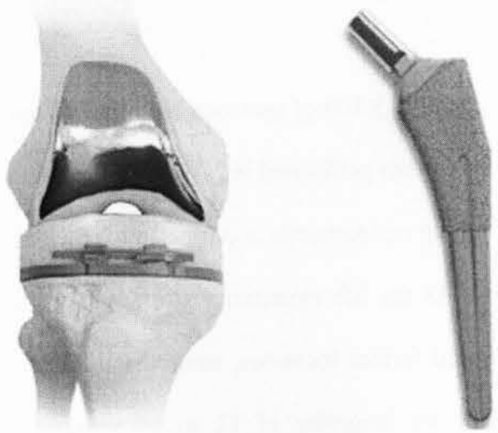

Figure 1.1 The hip and knee implants from Biomet.com [12].

One of the important considerations in the durability of the Ti-6Al-4V ELI implant is its resistance to fatigue due to the routine activities of walking, running and stair climbing. A typical implant or bone experiences up to 2×10^6 cycles annually [13]. Fatigue fracture has indeed been identified as one of the major problems associated with failure of medical devices [13-17]. As shown from Figure 1.2, the fatigue failure of the implants in a 27 year old woman weighing 74 kg and a 76 year old woman weighing 71 kg occurred seriously in their body after only 24 months in service [16].

The reported fatigue tests used to evaluate biomaterials basically involve the stress-controlled S-N fatigue behavior [1,14,18-20], and fracture mechanics based fatigue crack propagation behavior [14]. No strain-controlled low cycle fatigue (LCF) resistance data

of the Ti-6Al-4V ELI alloy has been seen in the literature. An objective of this investigation is to identify the LCF deformation characteristics of Ti-6Al-4V ELI alloy.

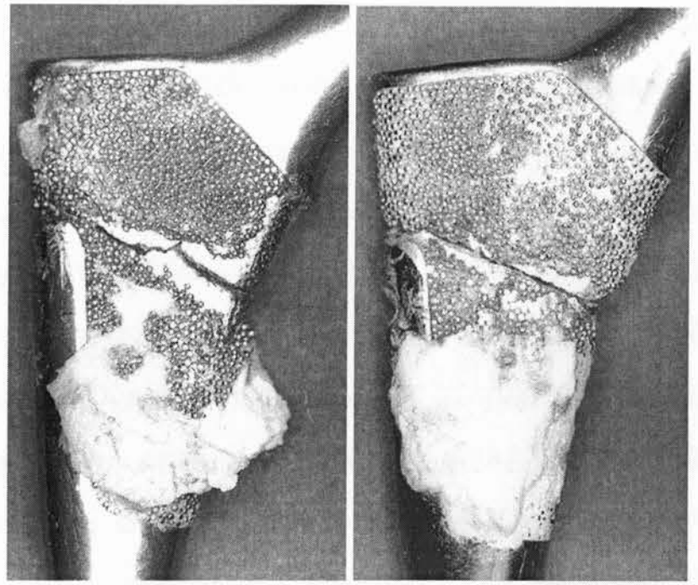

Figure 1.2 Fatigue fracture in an implant of (a) 27 year old woman weighing 74 kg (b) 76 year old woman weighing 71 kg [16].

On the other hand, where a contacting motion of counterparts is required, the relatively poor wear resistance of this alloy leads to excessive wear, mechanical and chemical instability, and implant loosening [2,8,21]. Various surface treatment methods, such as ion implantation, TiN coating, and thermal oxidation, have thus been proposed to improve the wear resistance by changing the nature of the surface [22]. The high reactivity of titanium and its alloys with nitrogen, oxygen, and carbon at high temperatures facilitate the use of these elements to improve the poor wear resistance of these materials. Nitriding and oxidizing are two of the most widely used techniques for

surface alloying with nitrogen and oxygen, as they lead to modified surface layers with improved hardness and wear resistance [23]. Thermal oxidation, carried out in a normal atmospheric condition containing oxygen and nitrogen, has recently been reported to be a promising approach for producing hard surfaces on Ti alloys [21,23,24-26], where a hardened oxygen diffusion zone formed beneath the TiO_2 layer provided good protection from corrosion and wear [24,27,28] and also improved the biocompatibility [24]. The effect of thermal oxidation on the wear resistance [21,26,28], corrosion and corrosion-wear behavior of a Ti-6Al-4V alloy [27,29] and stress-controlled high cycle fatigue [19,20] has recently been studied. This investigation is, therefore, aimed to evaluate the strain hardening exponent, strain rate sensitivity and LCF behavior of the Ti-6Al-4V ELI alloy subjected to varying heat treatment conditions with and without the thermal oxide layer.

CHAPTER TWO

Literature Review

2.1 Microstructure

At temperatures below 882°C, titanium has a hexagonal close packing (HCP) crystal structure, with a c/a ratio about 2% less than the ideal value of 1.633. Plastic deformation of HCP occurs by both slip and twinning [30]. These are common characteristics of unalloyed pure titanium. Titanium transforms to the β phase with a body centred cubic (BCC) crystal structure on heating to 882.5°C. If on cooling the BCC form is held just below the transformation temperature, HCP α phase forms from the β very slowly. At lower temperatures, the rate of transformation is more rapid. It is not possible to retain the β phase by sudden cooling no matter how rapid the quench [30].

The simplest type of titanium alloy is the all-α formed by the addition of an α stabilizer usually aluminium. Aluminium has a strong solid solution hardening effect on titanium. The α+β alloys, with a small β stabilizer, such as Ti+6%Al+4%V are also used at elevated temperatures [30]. The main focus of study in this thesis will be the ELI grade of Ti-6Al-4V alloy, with extra low interstitials of oxygen and nitrogen.

Titanium alloys containing β stabilizer additions can retain the β with appropriately rapid cooling from either the β or the α+β phase if the β contains sufficient stabilizer. The ability to retain the β phase is not the same for each alloying element. In Ti-V alloy, 16% of V is required [30].

The morphology, or shape, of α in an α+β alloy plays an important role in determining tensile ductility, resistance to fracture in the presence of a pre-existing crack and development of fatigue cracks [30].

The following micrographs represent some examples of the microstructure of Ti-6Al-4V alloy. Figure 2.1 illustrates Ti-6Al-4V alloy quenched from the β field, etched with benzol chloride + HF (hydrogen fluoride), producing martensite microstructure. Figure 2.2 shows Ti-6Al-4V alloy after furnace cooling from the β field into an α+β field at 930°C, held 46 h to coarsen the structure, water quenched, reheated to 770°C and again water quenched [30]. Figure 2.3 presents the microstructure of Ti-6Al-4V held at 930°C for 72h and water-quenched, reheated at 740°C for 2h and quenched. Equiaxed α (dark) formed at 930°C in a matrix of decomposed martensite. Figure 2.4 demonstrates the microstructure of Ti-6Al-4V held at 910°C for 20h, furnace cooled to 790°C, held 1 h and quenched resulting in the microstructure that consisted of equiaxed α (dark) and retained β (light) [30]. It is seen from Figure 2.1, Figure 2.2 and Figure 2.3 that β has been transformed to martensite on quenching, whether or not α is present, if the β is of proper composition [30].

Figure 2.1 *Ti-6Al-4V quenched from the β field, etched with benzol chloride + HF (hydrogen fluoride) [30].*

Figure 2.2 *Ti-6Al-4V alloy furnace cooled from the β field into the α+β field at 930°C, held 46 h, water quenched, reheated to 770°C and again water quenched [30].*

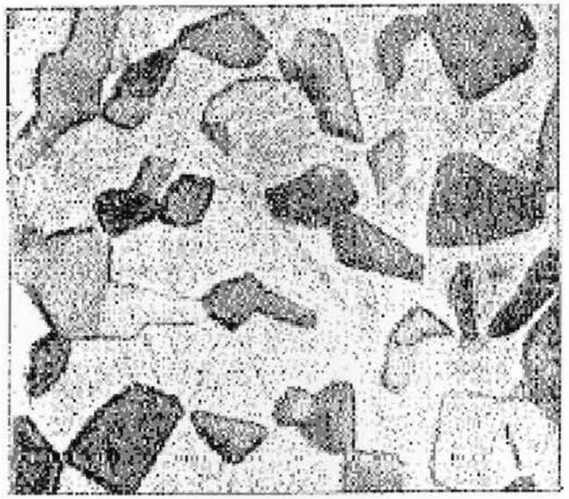

Figure 2.3 *Ti-6Al-4V alloy held at 930ºC for 72 h and water-quenched, reheated at 740ºC for 2 h and quenched [30].*

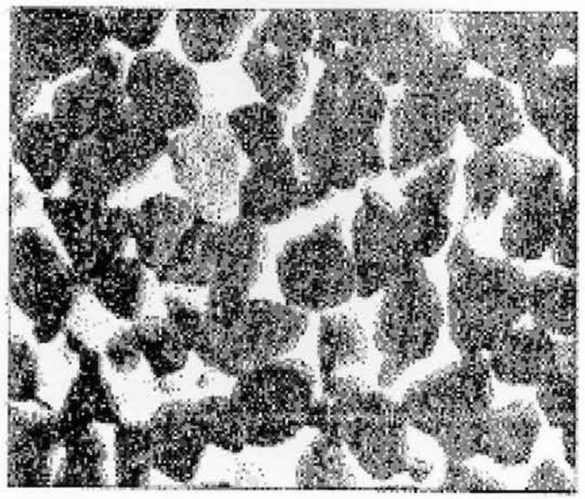

Figure 2.4 *Ti-6Al-4V alloy held at 910ºC for 20 h, furnace cooled to 790ºC, held 1 h and quenched [30].*

Primary α exists in two forms, widmanstatten plates and grain boundary α or equiaxed α. The widmanstatten structure forms on cooling either from the β, into the α+β field, to some lower temperature in the same two-phase field, as shown in Figure 2.2. An orientation relationship exists between the widmanstatten α plates, which form within the grains and the β grains in which they form. Equiaxed α will develop from the platelet form by hot working in the α+β field followed by recrystallization in the same two-phase field, but not necessarily at the same temperature used for hot working as shown in Figure 2.4 [30].

The α+β interfaces, in both widmanstatten and the equiaxed α, may serve as sites for void formation during tensile testing or during tensile fracture in the region ahead of a pre-existing crack. Both widmanstatten and equiaxed α particles having relatively long interfaces with β provide a ready path for void growth. Voids in the platelet structure reach a critical size for fracture at lower strains than they do in equiaxed structures, where the α particles also serve as crack stoppers [30]. Ti-6Al-4V ELI is primarily a α+β alloy, showing the characteristics of improved ductility and toughness because of reduced interstitial impurities [31].

2.2 Hardness

Hardness is one of the important mechanical properties of Ti-6Al-4V ELI alloy, because of its low wear resistance. As mentioned earlier, Ti alloys have tribological characteristics like high friction coefficient, small resistance to wear and high propensity to seizure [3]. To

overcome these problems researchers have used surface treatments to increase the hardness to generate surface hardened layer. Different surface hardening methods have been suggested, including a TiN coating on the surface by nitrogen glow discharge as the plasma source [32]. Figure 2.5 shows the hardness profiles obtained by Ueda *et al.* [32] for different times of treatments. At about 150 minutes of treatment, the hardness was about 25 GPa, or about 5 times the hardness of the untreated sample. The hardness improvement extends up to around 1.2 μm depth, decaying smoothly to the bulk hardness values. Furthermore, more than 2.5 times improvement could be achieved when the samples were treated at 400°C for one hour [32].

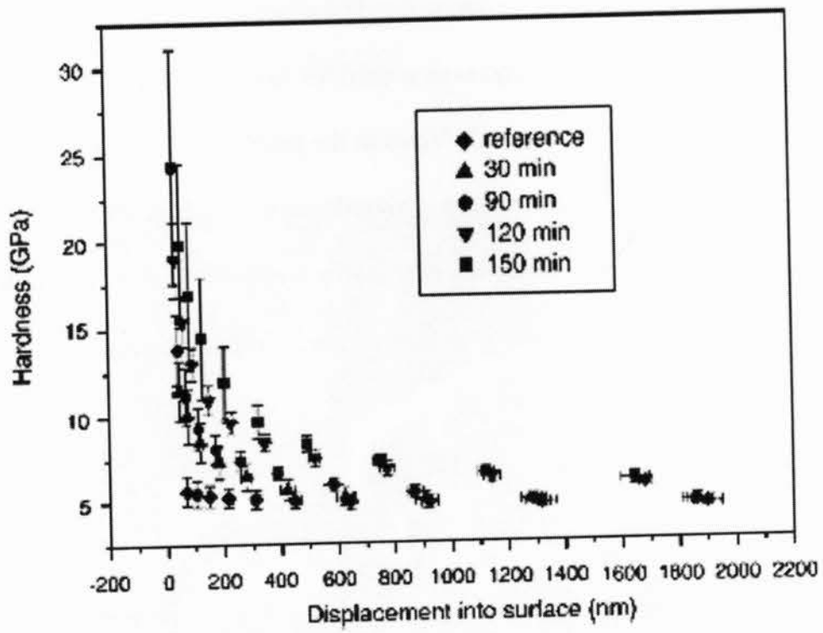

Figure 2.5 *Hardness profiles of Ti6Al4V treated by plasma immersion ion implantation at 800°C, at different treatment times [32].*

Dudek *et al.* [33] exposed the surface of the specimens to glow discharge plasma in an atmosphere composed of Ar and O_2 with two different oxygen concentrations, which resulted in surface regions of all the specimens hardened due to inward diffusion of oxygen. As shown in Figure 2.6, the diffusion treatment with the use of the glow discharge plasma in Ar + O_2 atmosphere may be an effective way to improve the tribological characteristics of Ti-6Al-4V alloy through an effective decrease in friction coefficient and increase of resistance to wear [33].The inset in figure 2.6 representing different diffusion hardening process namely, O (Air – atmosphere), A (90% Ar + 10%O_2 for 3 Hours), B(90% Ar + 10%O_2 for 6 Hours) and C (10% Ar + 90%O_2 for 6 Hours).

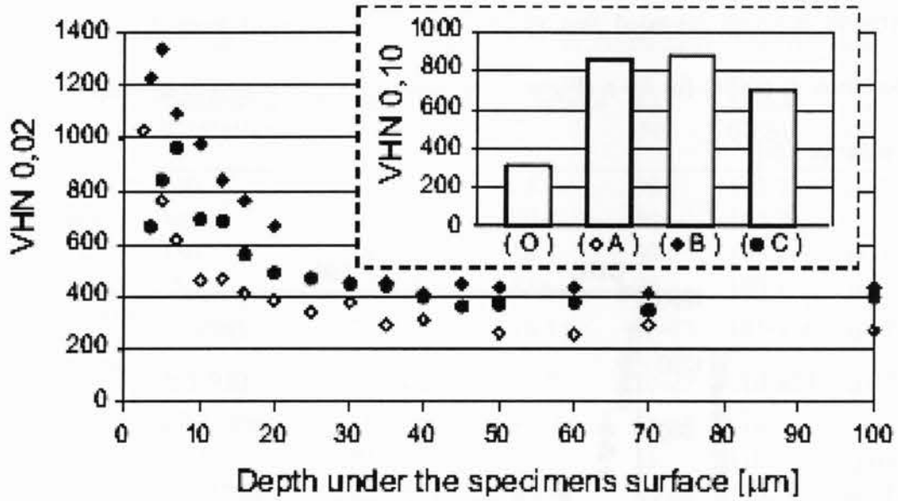

Figure 2.6 *Microhardness profiles (VHN 0.02) on cross-sections of specimens subjected to different treatments in the glow discharge plasma; in the inset, the surface microhardness (VHN 0.10) of the specimens is given as well [33].*

Santos *et al.* [34] evaluated the nano-hardness, elastic modulus and brittleness of titanium oxide (titania) films produced by anodic oxidation for biomedical applications. Corrosion resistance increased because of high affinity between titanium and oxygen, promoting a spontaneous formation of thin stable oxide layer on the Ti-surface. Their results showed that oxide films were less ductile [34]. Gulyeruz and Cinemoglu [29] stated that thermal oxidation carried out in a normal atmospheric condition containing oxygen as well as nitrogen appeared to be very promising for producing hard surfaces on Ti-alloys. In their study, they examined the effect of thermal oxidation on the dry sliding wear resistance of a Ti-6Al-4V alloy. Oxidation introduced hard surface layers composed of TiO_2 and oxygen diffusion zone beneath it. A hardness survey conducted under a load of 10 g with a Vickers pyramid indenter revealed that surface hardness increased from 450 to 1300 HV upon oxidation at 600°C for 60 h (Figure 2.7), accompanied by significant improvement in wear resistance [29].

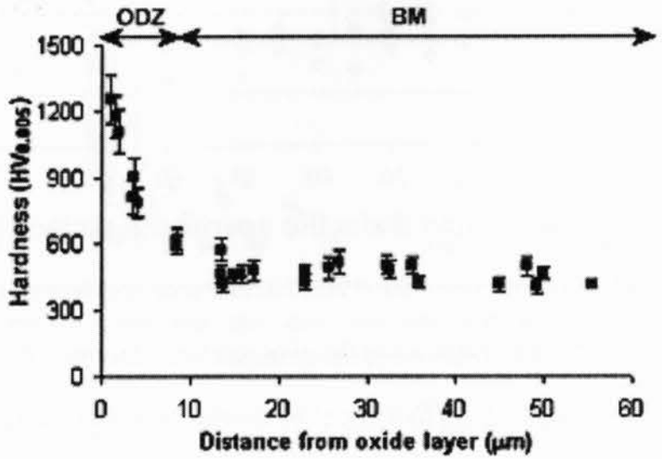

Figure 2.7 *hardness-depth profile of the sample oxidized for 60 h (ODZ: oxygen diffusion zone; BM: base metal) [29].*

2.3 Tensile and fatigue data

The mechanical properties of the titanium alloys developed for implant applications to date were described by Ninoomi [10] are shown in Table 2.1. Pure titanium and titanium alloys are still the most attractive metallic materials for biomedical applications, in which Ti-6Al-4V ELI alloy has been the main biomedical titanium alloy for a long period even though new Ti alloys are being developed.

Table 2.1 *Mechanical properties of titanium alloys for biomedical applications [10].*

Alloy	Tensile Strength (UTS) (MPa)	Yield Strength (MPa)	Elongation (%)	RA (%)	Modulus (GPA)	Type of alloy
Pure Ti grade1	240	170	24	30	102.7	α
Pure Ti grade2	345	275	20	30	102.7	α
Pure Ti grade3	450	380	18	30	103.4	α
Pure Ti grade4	550	485	15	25	104.1	α
Ti-6Al-4V ELI (mill annealed)	860-965	795-875	10-15	25-47	101-110	α+β
Ti-6Al-4V ELI (annealed)	895-930	825-869	6-10	20-25	110-114	α+β
Ti-6Al-7Nb	900-1050	880-950	8.1-15	25-45	114	α+β
Ti-5Al-2.5Fe	1020	895	15	35	112	α+β
Ti-5Al-1.5B	925-1080	820-930	15-17	36-45	110	α+β
Ti-13Nb-13Zr (aged)	973-1037	836-908	10-16	27-53	79-84	β
Ti-12Mo-6Zr-2Fe	1060-1100	1000-1060	18-22	64-73	74-85	β
Ti-15Mo (annealed)	874	544	21	82	78	β
Tiadyne 1610 (aged)	851	736	10		81	β

Gungor *et al.* [35] conducted the tensile and fatigue tests of Ti-6Al-4V of the standard and ELI grades in the form of seamless tubes for different material conditions and their results are tabulated in Table 2.2 and Table 2.3.

Table 2.2 Tensile properties of Ti–6Al–4V seamless tubes [35].

Materials	Ti-6Al-4V (grade)	Material condition	UTS (MPa)	YS (MPa)	Elongation (%)	Reduction Area (%)
β Extrusion	Standard	Annealed	960 ± 5	857 ± 5	13 ± 0	26 ± 1
α+β Extrusion	Standard	Annealed	981 ± 5	910 ± 11	15 ± 1	37 ± 1
Rotary Piercing	Standard	Annealed	999 ± 6	884 ± 6	13 ± 1	27 ± 2
Flowforming	Standard	As-flowformed	1246 ± 8	968 ± 11	12 ± 2	28 ± 9
Flowforming	ELI	As-flowformed	1170 ± 6	908 ± 63	14 ± 2	40 ± 7
Flowforming	ELI	Stress-relieved	1221 ± 4	1161 ± 7	12 ± 1	34 ± 7

Table 2.3 Fatigue properties of Ti–6Al–4V seamless tubes [35].

Max. Stress (MPa)	Fatigue life (cycles)							
	β Extrusion-annealed standard grade		α+β Extrusion-annealed standard grade		Rotary piercing-annealed standard grade		Flowforming-stress relieved ELI grade	
550	23,147	24,038	27,665	29,993	23,114	25,926	47,823	52,848
517	28,257	36,883	30,298	43,051	29,646	38,623		-
482	35,162	37,170	33,546	46,920	27,355	68,092	53,461	116,420
448	63,405	64,285	51,777	64,833	56,154	63,109		-
413	42,050	250.941	49,837	107,439	61,902	93,800	11,790	141,471
379	64,833	78,118	69,200	77,395	303,399	629,331		-
345	876,520	903,163	8,825,591	-	5,149,332	5,149,332	10,151,527*	10,265,305*

* Run out.

Akahori and Niinomi [15] examined the tensile and fatigue properties of Ti-6Al-4V ELI alloy with equiaxed α structure, where the hot rolled plates were subjected to heat treatment at 950°C followed by air cooling and aging at 813K in a vacuum, which produced an equiaxed α structure. These specimens were first fatigued under constant cyclic loading and

were unloaded after varying number of cycles and then the tensile tests were conducted. It was seen that the tensile strength of fatigued specimens of Ti-6Al-4V ELI with equiaxed α structure increases rapidly within the low cycle fatigue region. On the other hand, the elongation of fatigued specimens tested at various fatigue increments decreases rapidly within the low cycle fatigue region. The energy absorbed by fatigued specimens during various fatigue steps decreases rapidly in the late stages of the low cycle fatigue region. Furthermore, a hardness gradient develops initially from the surface to the inside of the specimens, and then in the later stages of fatigue, the internal hardness is equal to the surface hardness. The sub-structures both near and far from the surface of fatigued specimens, observed after various fatigue steps, show an increased dislocation density. However, at the late stages in low cycle fatigue region, the dislocation density far from the specimen surface also increases dramatically [15].

Tensile properties of fatigued specimens at a number of fatigue cycles are shown in Figure 2.8. In the low cycle fatigue region, the tensile strength increases rapidly; the 0.2% proof stress is nearly equal to the tensile strength at the later stages of the low cycle fatigue region. The increase in each strength is attributed to work hardening. At this late stage of the low cycle fatigue region, the tensile strength and 0.2% proof stress increase by about 6 and 12%, respectively, when compared with those of non-fatigued specimens [15].

Naughton and Tiernan [3], conducted tensile experiments on extra low interstitial (ELI) grade of Ti-6Al-4V alloy, with a nominal diameter of 2.36 mm. The stress-strain behavior of the alloy was examined at various temperatures ranging from 750 °C to 1050 °C. It was

determined that the flow stress is strain rate dependent, with a decrease in strain rate leading to a decrease in the associated flow stress as seen from Figure 2.9, Figure 2.10 and Figure 2.11. It was also clear that an increase in temperature decreased the associated flow stress, which can be attributed to adiabatic heating.

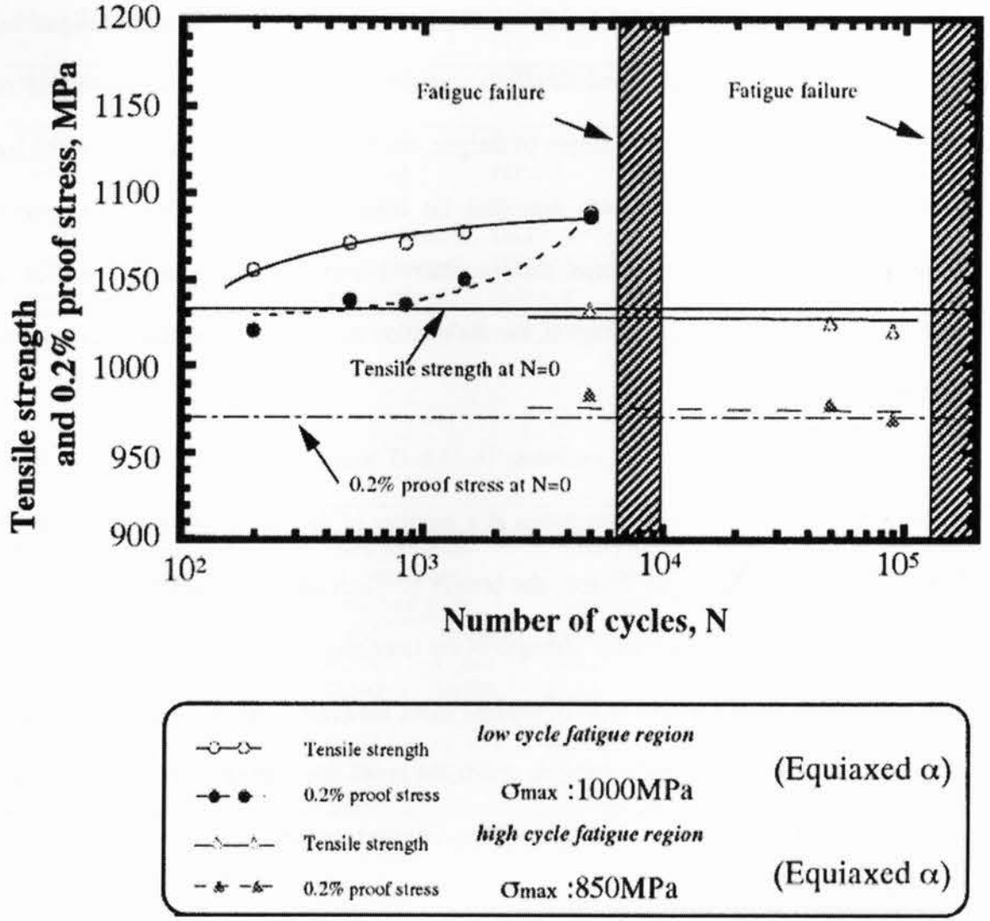

Figure 2.8 *Relationship between residual tensile strength or 0.2% proof stress after fatigue, as a function of number of cycles [15].*

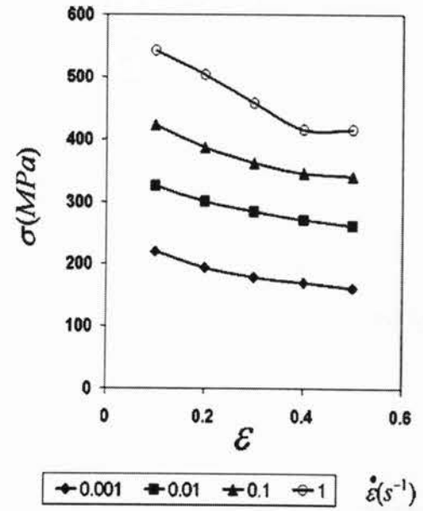

Figure 2.9 *Flow stress versus strain behavior of ELI grade Ti-6Al-4V at 750°C at various strain rates [3].*

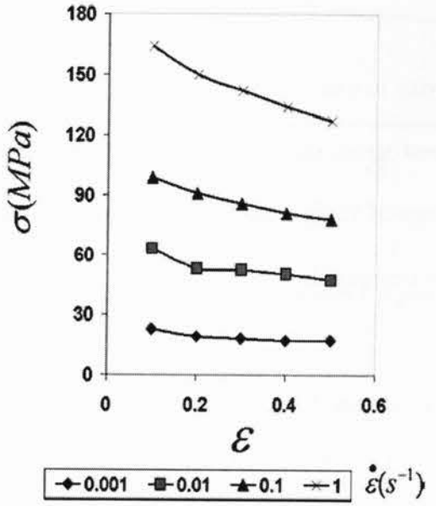

Figure 2.10 *Flow stress versus strain behavior of ELI grade Ti-6Al-4V at 950°C at various strain rates [3].*

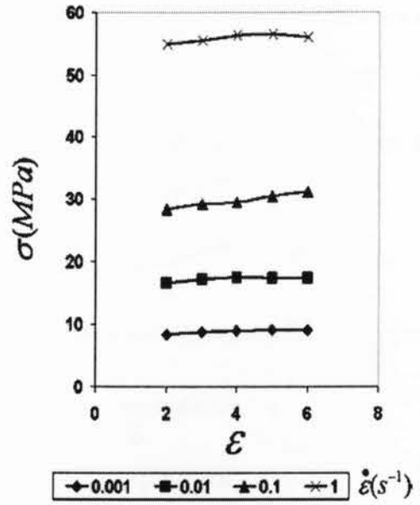

Figure 2.11 Flow stress versus strain behavior of ELI grade Ti-6Al-4V at 1050°C at various strain rates [3].

The strain rate sensitivity *m* values were then plotted against the strain rate, as presented in Figure 2.12. The highest strain rate sensitivity value *m* was determined to be 0.45 and this occurred at a temperature of 950°C. The results indicated that as the strain rate increased, the strain rate sensitivity *m* decreased.

So far there are only limited results reported on the strain rate sensitivity and strain hardening exponent for the ELI grade of Ti-6Al-4V alloy, especially with a hardened oxide layer. The objective of this investigation was to evaluate the mechanical properties of heat treated Ti-6Al-4V ELI alloy by varying the microstructure via heat treatment with or without the oxide layer by conducting tensile tests at various strain rates and low cycle fatigue tests. The results are reported in the ensuing chapters. Tensile results are presented in chapter 4, fatigue results are reported in chapter 5 and the relation between fractal dimension and fracture surface

roughness using a unique three dimensional fractal measuring technique is presented in chapter 6.

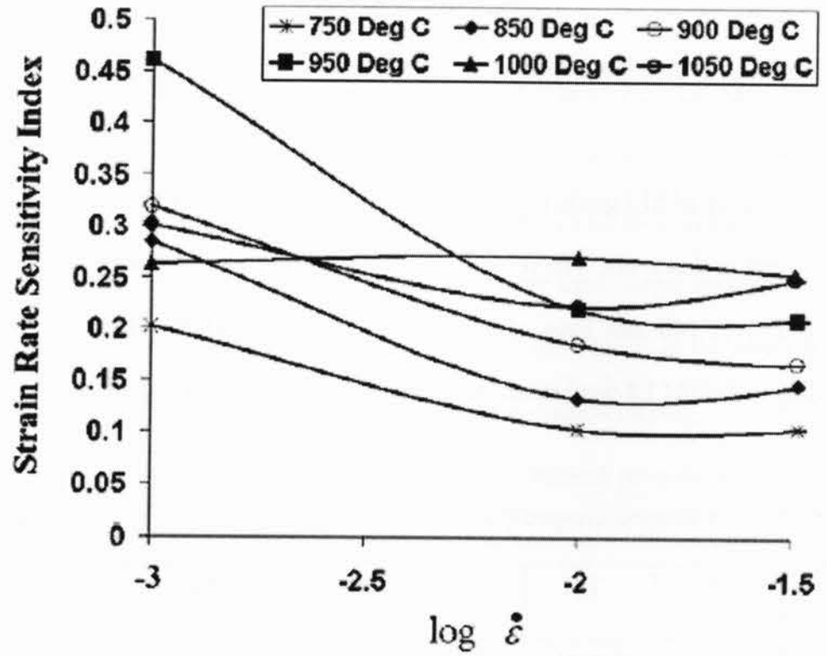

Figure 2.12 The strain rate sensitivity index m at various temperatures and key strain rates [3].

CHAPTER THREE

Material and Experimental Procedure

3.1 Material and heat treatment

Ti-6Al-4V alloy of ELI grade in an initially annealed condition with a thickness of 3.125 mm was selected in this study. The composition is shown in table 3.1. Subsized tensile specimens (Figure 3.1) of 140 mm long with a gauge length of 25 mm and gauge width of 6 mm according to ASTM E8 were machined in the rolling direction using a CNC machine.

Table 3.1 Chemical composition of as-received Ti-6Al-4V ELI alloy (weight percent).

N	C	H	Fe	O	Al	V	Ti
0.004	0.010	0.0052	0.18	0.10	5.90	4.06	Balance

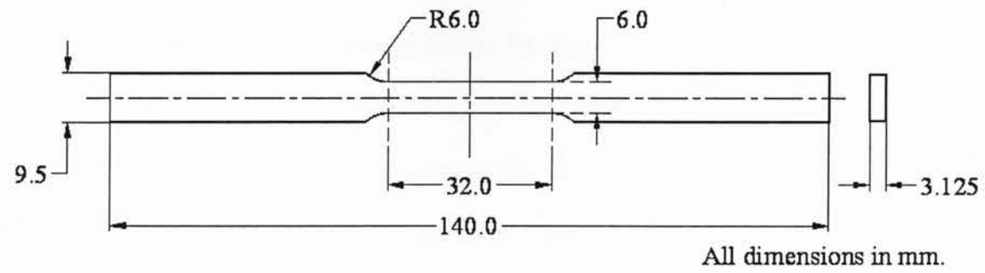

Figure 3.1 Geometry and dimensions of the tensile and fatigue specimens used in the present study.

Figure 3.2 shows a typical phase diagram of the Ti-6Al-4V alloy, basically an $\alpha+\beta$ alloy, which transforms to β when heated to above the transus temperature of 975°C. The heat treatment procedure is shown in Figure 3.3. Heat treatment was carried out at a temperature of 955°C for 30 minutes in an argon environment using a Lindberg atmosphere furnace, which was calibrated with chromel-alumel thermocouples in accordance with the AMS2750 standard. To control the thickness of the thermal oxide layer, the heat treatment was conducted with the argon atmosphere at a low flow rate of 15 CFH. Three cooling conditions – water quenching, air cooling, and furnace cooling were used. Some specimens were then subjected to aging treatments at a temperature of 525°C for 4 hours in the argon atmosphere at a flow rate of 15 CFH. Post-heat treatment process included cleaning and removing burrs. To reveal the effect of thermal oxide layer on the mechanical properties, some specimens were pickled using 5% HF + 20% HNO_3 solution to remove the oxidized alpha case layer for about 0.2 mm [36].

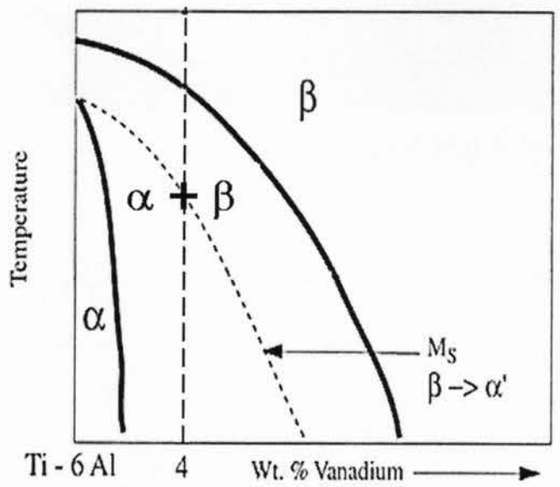

Figure 3.2 Typical phase diagram of Ti-6Al-4V alloy

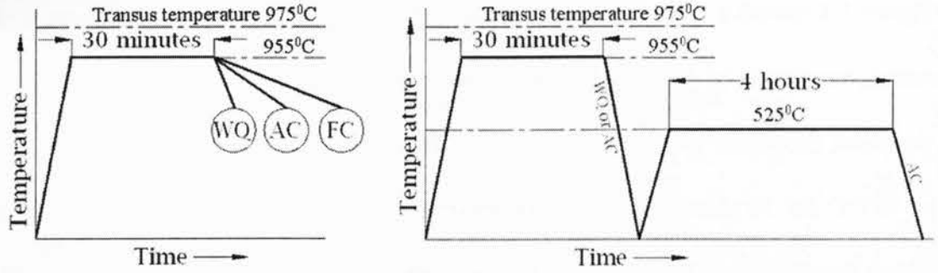

Figure 3.3 Schematic illustration of heat treatment procedure.

3.2 Microstructure and hardness tests

The as-received and heat-treated specimens were mounted using bakelite powder, ground with SiC papers of different grades, polished using 6μ diamond paste and Master prep solution, and etched with Kroll's reagent (2%HF+4%HNO_3). The microstructure was observed using a Nikon light microscope. The Knoop hardness values were determined using a computerized Buehler microhardness tester under 200 grams.

3.3 Tensile and fatigue tests

All samples were hand-ground progressively along the loading direction with 120, 320, and 600 emery papers to achieve a smooth surface. Both pickled and un-pickled specimens oriented in the rolling direction were subjected to tensile tests using a computerized Instron Instron 8801 servo-hydraulic testing system (Figure 3.4) at strain rates between 1×10^{-2} s^{-1} and 1×10^{-5} s^{-1}.

Low cycle fatigue (LCF) tests were performed under total strain control in a computerized Instron 8801 servo-hydraulic testing system. In the total strain-controlled fatigue testing, a triangular waveform with a strain ratio of R = -1 was applied at a constant strain rate of 1×10^{-2} s^{-1}. The fatigue tests at low total strain amplitudes were operated until 1×10^{4} cycles, and then changed to load control at a frequency of 50 Hz using sine waveform. Total strain amplitudes of 0.2%, 0.3%, 0.4%, 0.6% and 0.8% were applied in the LCF tests.

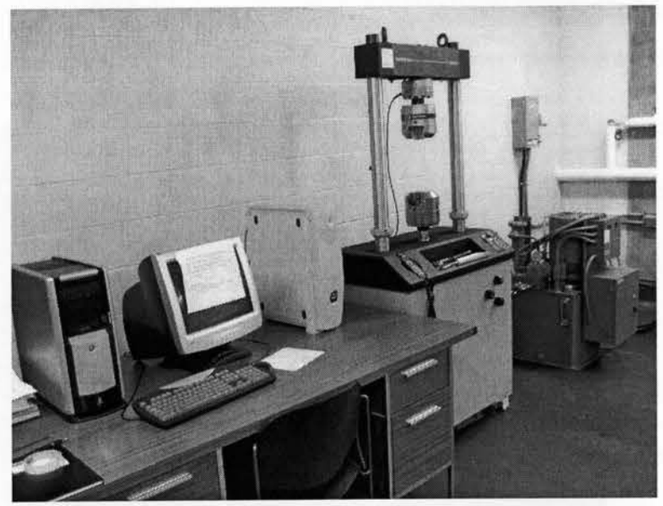

Figure 3.4 Picture of Instron 8801 servo-hydraulic testing system.

3.4 Fractography and fractal analysis

Fracture surfaces after testing were examined using a scanning electron microscope (SEM) coupled with energy dispersive X-ray spectroscopy (EDS) as shown in Figure 3.5 to identify the crack initiation sites and propagation mechanisms.

Fractal dimensions were determined via three-dimensional (3D) measurements of fracture surface areas versus the ruler scale (i.e., the side length of equilateral triangular tiles) using MeX software. The images of fracture surfaces used for the fractal analysis were taken near the centre and joined to form a 3D image at a magnification of 1000 times. Three 3D images were analyzed for each material condition after converting them into a digital elevation model (DEM) using a cut-off wavelength of 15λ, where λ is the profile filter which is the intersection between the waviness and roughness components, in micrometers. A detailed analysis is presented in chapter 6.

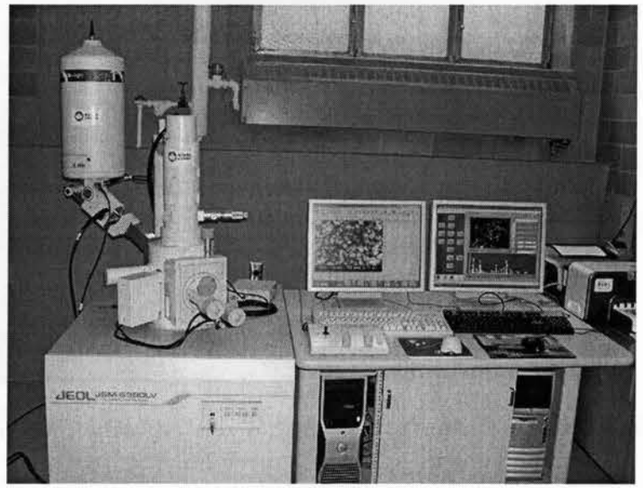

Figure 3.5 *Picture of Scanning electron microscope (SEM) coupled with energy dispersive X-ray spectroscopy.*

CHAPTER FOUR

Tensile Properties

4.1 Microstructure and microhardness

The microstructures of the Ti-6Al-4V ELI alloy in the as-received and heat-treated conditions are shown Figure 4.1. It is seen from Figure 4.1(a) that the microstructure of the as-received material consisted of primary α and $\alpha+\beta$ phases. After water quenching from 955°C, the microstructure consisted of primary α and $\alpha'+\beta$ as shown in Figure 4.1(b). Semiatin and Bieler [37] confirmed this in their experiments on Ti-6Al-4V alloy and reported that the breakdown of the microstructure took place in the two-phase field, below the β transus temperature at which the β became $\alpha+\beta$. The formation of martensite from β phase at 955°C was due to the fast cooling rate during water quenching, as reported by Zhang *et al.* [38] for the Ti-6Al-4V alloy. They explained that phase transformation occurred from the high temperature β-Ti to low temperature α-Ti (diffusion controlled when slow cooling) or α'-Ti (shear dominated when rapid cooling). This is in agreement with the microstructure described by Donachie, Jr. [39]. Jovanovic *et al.* [40] also reported a similar microstructure after heat treatment of Ti-6Al-4V alloy at 950°C followed by water quenching. Figure 4.1(c) shows the microstructure obtained after air cooling from 955°C, which resulted in a mixture of acicular α and β with primary α, similar to the result obtained by Jovanovic *et al.* [40] and also described by Donachie, Jr. [39]. After furnace cooling from 955°C (Figure 4.1(d)), the

microstructure consisted of equiaxed α and intergranular β. Such a microstructure was also obtained by Donachie, Jr. [39], Jovanovic *et al.* [40] and Kruger *et al.* [41]. Figure 4.1(e) shows the microstructure obtained after air cooling from 955°C and subsequent aging which resulted in a mixture of acicular α and β with primary α, similar to the result obtained by Jovanovic *et al.* [40] and also described by Donachie, Jr. [39]. After water quenching from 955°C and subsequent aging at 525°C (Figure 4.1(c)), the microstructure consisted of primary α and α'+β. The subsequent aging resulted in precipitation of some fine secondary α phase in the metastable β phase [41].

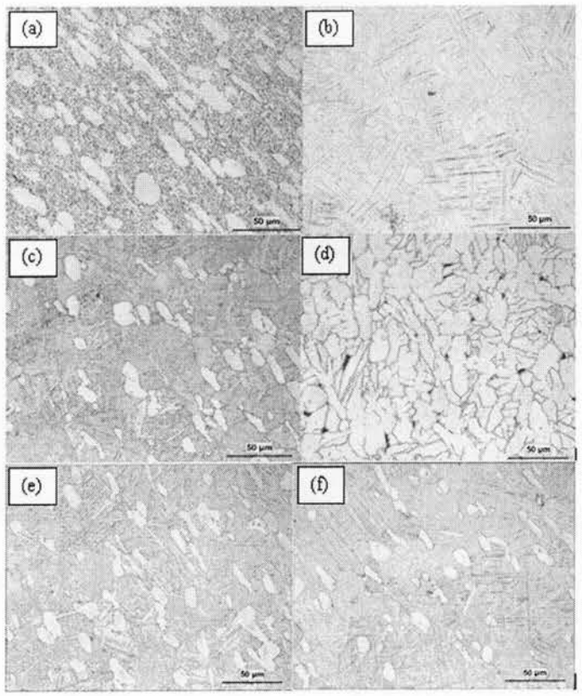

Figure 4.1 *Microstructures of Ti-6Al-4V ELI alloy in different conditions, (a) as-received, (b) water quenching (WQ), (c) air cooling (AC), (d) furnace cooling (FC) (e) AC +aging and (f) WQ + aging.*

Figure 4.2 shows the microhardness profile from the surface to the inside of the specimen. It is seen that the highest hardness value occurred at the surface of the specimens, indicating that the surface has effectively been hardened. Similar results on the microhardness profile were also reported in [21,23,27]. The specimen subjected to water quenching (WQ) exhibited much higher hardness values, while the furnace cooling (FC) led to the lowest hardness out of all the conditions considered in this study. This is in agreement with the results obtained by Jovanovic *et al.* [37] for Ti-6Al-4V alloy. Kruger *et al.* [41] reported that microstructures obtained by annealing below the β-transus followed by FC showed lowest hardness values, the balanced properties of high deformability and strength and highest energy consumption for the Ti-6Al-4V alloy. In general, the hardness increases as the rate of cooling increases. This is due to the formation of martensite arising from rapid cooling [38,39,42,43]. The hardness of the specimen subjected to air cooling (AC) lies in-between those of the WQ and FC. It is also seen that the AC specimen had a slightly higher hardness than the as-received specimen. This could be understood on the basis of the difference in the microstructures shown in Figure 4.1(a) and (c), where the acicular α + β microconstituent and fewer primary α phase occurred after AC (Figure 4.1(c)) while non-acicular α + β microconstituent and more primary α phase were present in the as-received specimen (Figure 4.1(a)). Concerning the effect of the shape of the microstructures, the plate-shaped (or acicular) microstructure had normally higher resistance to the dislocation movement or plastic deformation, thus leading to a higher hardness. It is also seen from Figure 4.2 that there was a slight increase in the hardness close to the surface in the as-received specimen, but it was much lower than the surface hardness of the heat-treated specimens.

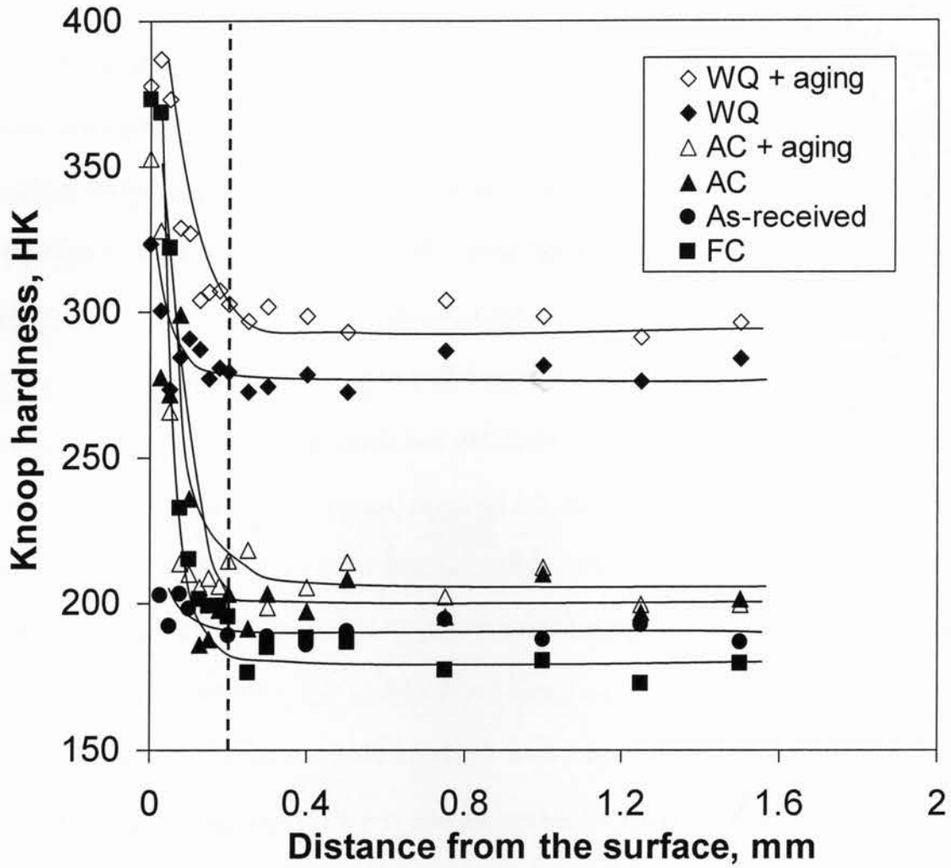

Figure 4.2 Knoop microhardness profile of the Ti-6Al-4V ELI alloy in all conditions.

4.2 Effect of heat treatment on the tensile properties

Figure 4.3 illustrates the stress-strain curves obtained for the AC + aging specimens with and without pickling tested at a strain rate of 1×10^{-4} s^{-1}. It is seen that the hard oxidized layer of about 0.15 mm had a minor effect on the yield strength and led to only a slight decrease in

the ultimate tensile strength (UTS), despite the reduction in the ductility. This was in agreement with the results of the Ti-6Al-4V alloy reported by Zhu *et al.* [44] who stated that the oxide scale can induce clefts and degrade the ductility while having little effect on the yield strength and UTS of the alloy. The following results presented will thus be based on the tests of specimens without pickling.

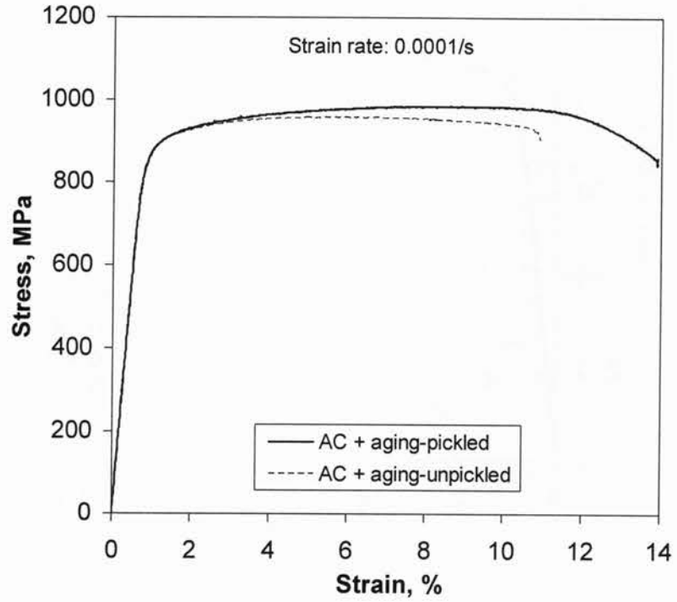

Figure 4.3 Stress-strain curves in the AC + aging condition with and without pickling tested at a strain rate of 1×10^{-4} s^{-1}.

Figure 4.4 shows the stress-strain curves for the AC + aging condition tested at different strain rates. The stress-strain curve moved higher as the strain rate increased, leading to higher YS and UTS, and lower ductility. Semiatin and Bieler [37] have reported similar

results for non-ELI grade of Ti-6Al-4V alloy. The dependence of the flow stress of Ti-6Al-4V ELI alloy on the strain rate may be described using a power-law [45],

$$\sigma = C\dot{\varepsilon}^{m}, \tag{4.1}$$

where σ is the flow stress, C is a constant and m is the strain-rate sensitivity.

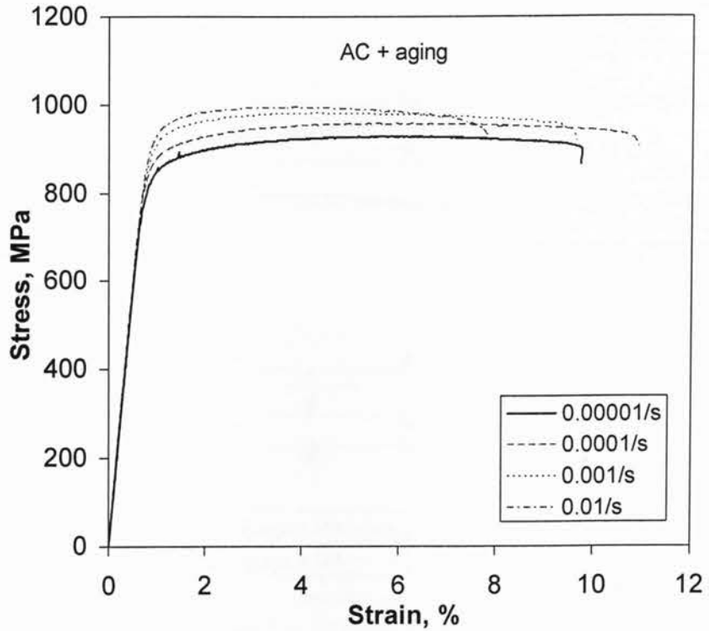

Figure 4.4 Stress- strain curves versus the strain rates in the AC + aging condition.

The influence of heat treatment conditions on the stress-strain curves at a strain rate of 1×10^{-3} s^{-1} is shown in Figure 4.5. The WQ + aging condition gave rise to the highest value of the stress but the lowest ductility. This is attributed to the formation of the martensitic microstructure induced by WQ. In comparison with the internal average microhardness shown in Figure 4.2, there was a clear correspondence between the hardness and the tensile strength shown in Figure 4.5. It is also seen that, unlike the heat-treated specimens, the as-

received specimen exhibited an abrupt yielding, giving rise to a slightly higher YS, compared to the AC condition (Figure 4.6).

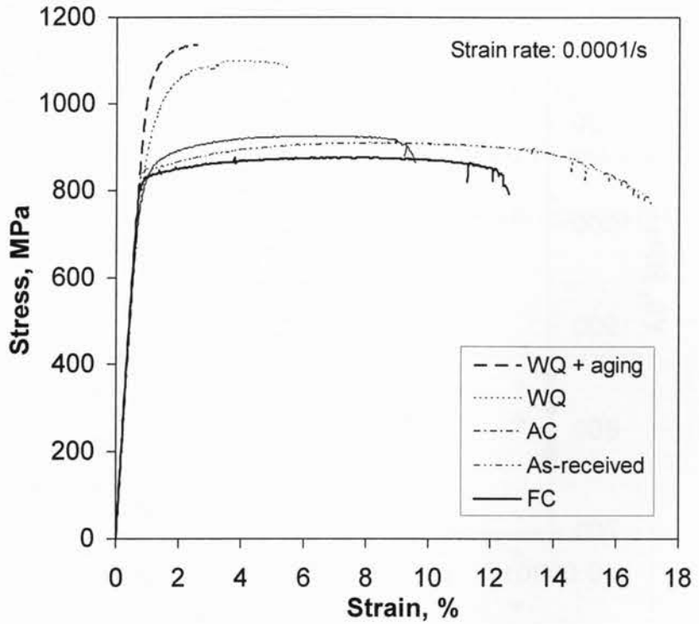

Figure 4.5 Stress-strain curves of Ti-6Al-4V ELI alloy in different heat treatment conditions tested at a strain rate of 1×10^{-3} s^{-1}.

The effect of the strain rate on the YS for the Ti-6Al-4V ELI alloy in all the six material conditions is shown in Figure 4.6. With increasing strain rate, the yield strength increases. The WQ+AG and WQ resulted in a higher YS. This trend is consistent with the results reported by Semiatin and Bieler [37] and Jovanovic *et al.* [40]. In another study of Ti alloys, Soares *et al.* [46] also reported that the greater strength of the WQ material was due to the rapid cooling in water or oil, where the β phase was transformed into a stronger martensite

after quenching in water above 800°C. The grain size is also related to the velocity at which the material was cooled, and, in general, rapid cooling promotes finer structure.

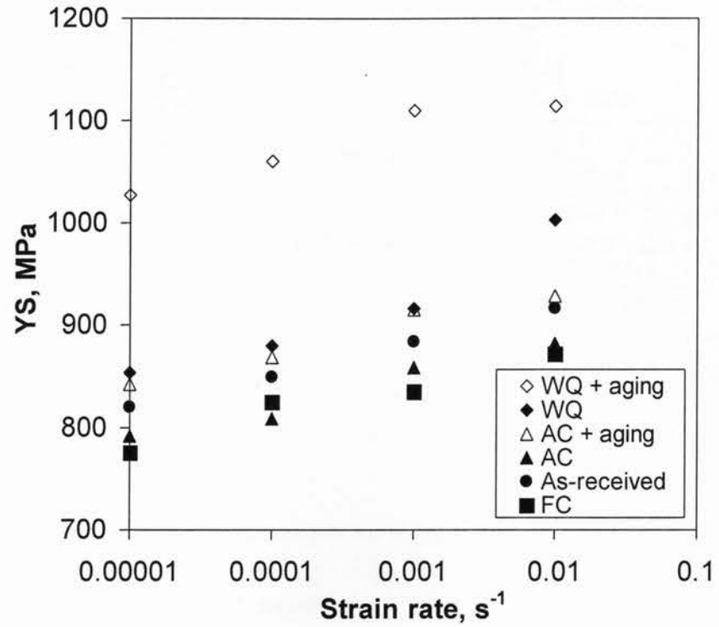

Figure 4.6 *Effect of strain rate on the yield strength of Ti-6Al-4V ELI alloy in different heat treatment conditions.*

The effect of the strain rate on the UTS of this alloy in different heat treatment conditions is shown in Figure 4.7. Again, the UTS increased with increasing strain rate, and the hardest material subjected to WQ + aging corresponded to the highest UTS. This is in agreement with the results reported by Semiatin and Bieler [37], where the peak stress increased with decreasing alpha platelet thickness, and the peak stress was also highest for the martensitic microstructure in the Ti-6Al-4V alloy quenched from 955°C. Figure 4.8 shows the variation of the ductility with the strain rate for the six material conditions. As expected, the ductility

decreased with increasing strain rate, and the hardest material corresponded to the lowest ductility. Similar results were also reported by Jovanovic *et al.* [40] who mentioned that the effect of α' and α was the major contributor for these trends. Kwon *et al.* [47] reported similar results where the highest ductility corresponded to a discontinuity of the α phase (in which slip can easily occur) because of the impediment of the β phase. The furnace cooled specimen did not correspond to a high ductility which could be understood because of the very large brittle oxide layer (Figure 4.2) causing a reduction in ductility [44].

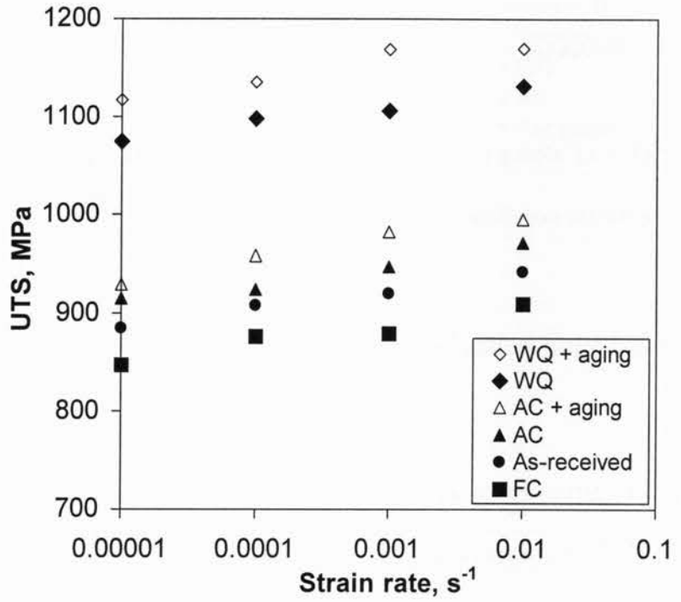

Figure 4.7 *Effect of strain rate on the ultimate tensile strength of Ti-6Al-4V ELI alloy in different heat treatment conditions.*

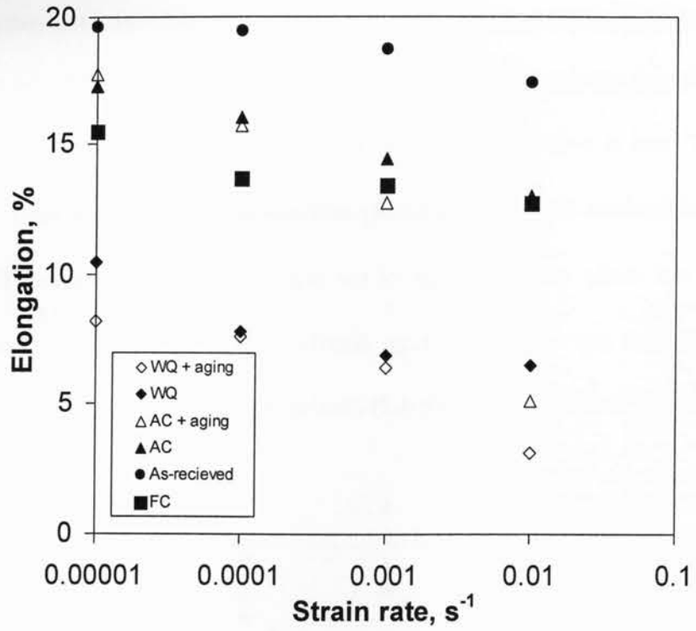

Figure 4.8 *Effect of strain rate on the ductility of Ti-6Al-4V ELI alloy in different heat treatment conditions.*

4.3 Strain hardening behavior

After yielding, the stress-strain relationship in the uniform deformation stage may be expressed by the Hollomon equation,

$$\sigma = K\varepsilon^n , \qquad (4.2)$$

where σ is the true stress, ε is the true strain, n is the strain hardening exponent, and K is the strength coefficient. The evaluated n values following equation (4.2) as a function of the strain rate are shown in Figure 4.9. It is seen that the n values decreased with increasing strain rate. Similar results were reported by Jain *et al.* [48] and El-Domiaty [49] for the non-

ELI Ti-6Al-4V alloy. Tang *et al.* [50] reported similar results for metallic materials and gave the following relationship between strain-hardening exponent (n) and the strain rate ($\dot{\varepsilon}$),

$$n = n_0 - b\log_{10}\dot{\varepsilon} , \qquad (4.3)$$

where n_o is a material constant, and b is the slope in the n vs. $\log_{10}\dot{\varepsilon}$ graph. As the strain rate increased, the strain-hardening exponent decreased proportionally in the semi-log scale. While the overall decreasing trend of n values with increasing strain rate could be described by equation (4.3), it appeared difficult to identify the effect of heat treatment conditions.

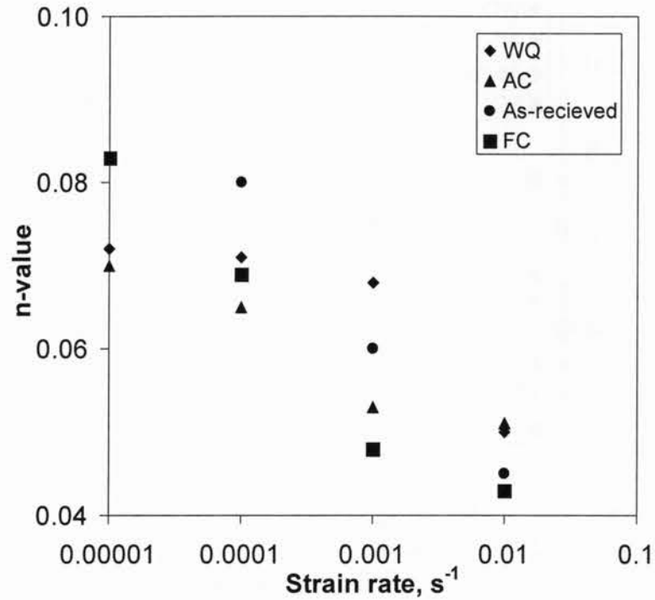

Figure 4.9 *Strain hardening exponent n evaluated on the basis of Hollomon equation as a function of strain rate in the different conditions.*

To get a clear picture, it was decided to evaluate the strain hardening exponent based on the Ludwig equation,

$$\sigma - \sigma_y = K\varepsilon^{n1} \qquad (4.4)$$

where σ_y is the yield strength, K_1 is the strength coefficient and n_1 is the strain-hardening exponent. Figure 4.10 shows the strain hardening exponent n_1 versus the strain rate for the four material conditions based on the Ludwig equation. While the n_1 values did not seem to show a decreasing trend of n values, the n_1 values were much larger than the n values. The heat treatment led to a decrease in the n_1 values, with the n_1 values in the FC condition closest to those of the as-received condition. The n_1 values in the WQ condition were the lowest, and the n_1 values in the AC condition lay in-between those in the FC and WQ conditions.

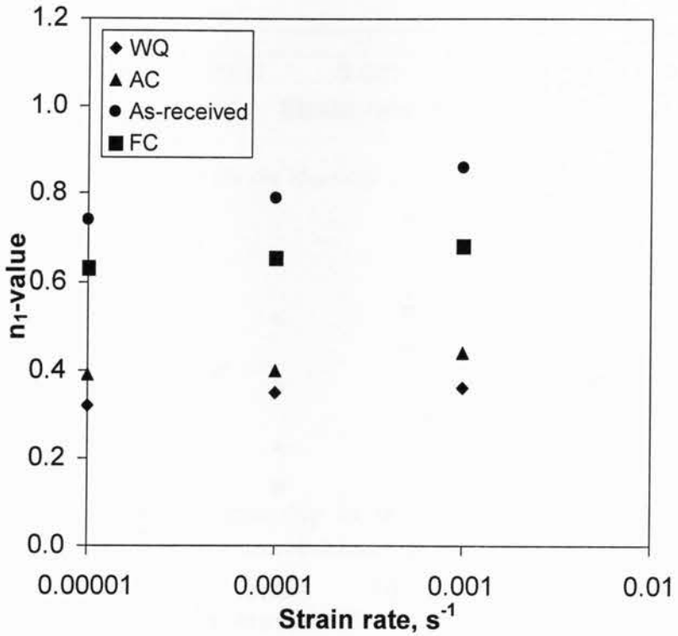

Figure 4.10 Strain hardening exponent n_1 evaluated on the basis of Ludwig equation as a function of strain rate in the different conditions.

Figure 4.11 shows the effect of the strain rate on the strain hardening exponent evaluated on the basis of a modified relationship proposed by Afrin *et al.* [51],

$$\sigma - \sigma_y = K(\varepsilon - \varepsilon_y)^{n^*}, \qquad (4.5)$$

where σ_y is the yield strength, ε_y is the yield strain, K is a constant and n^* is the strain hardening exponent. It is obvious that the elastic component in both stress and strain is eliminated in equation (4.5). It is seen again that the as-received condition also exhibited the highest strain hardening exponent, followed by the FC, AC and WQ conditions. The n^* values evaluated on the basis of equation (4.5) are much larger than the n values evaluated based on equation (4.2), but slightly smaller than the n_1 values based on equation (4.4). Similar relative values of the three strain hardening exponents were also seen in [51].

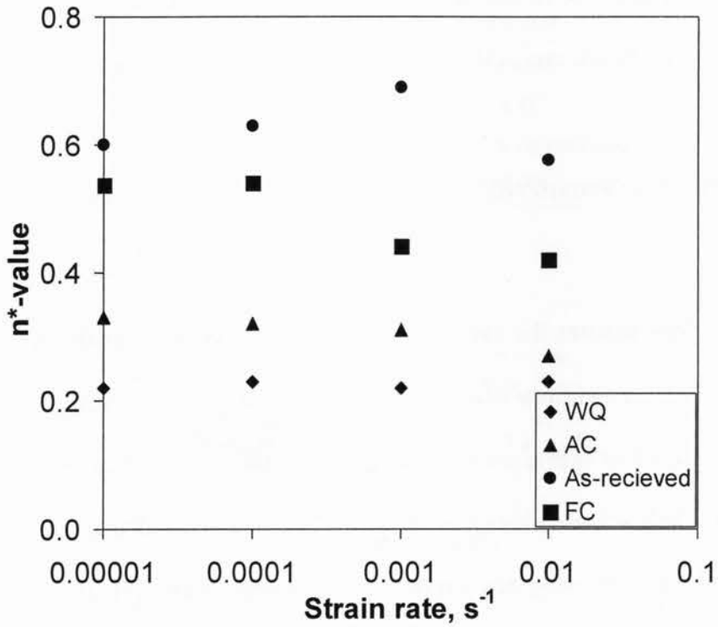

Figure 4.11 Strain hardening exponent n^* as a function of strain rates in the different conditions.

The work hardening rate as a function of true stress for the Ti-6Al-4V ELI alloy in the four material conditions tested at a strain rate of 0.0001 s^{-1} is shown Figure 4.12. In spite of the low strain hardening exponent (Figure 4.9-4.11) evaluated over the uniform deformation

range, the WQ specimen exhibited a much higher initial work hardening rate after yielding occurred. This was attributed to the higher dislocation densities generated in the martensitic structure (Figure 4.1(b)), which was observed by Markandeya *et al.* [52] in Cu-Ti-Cd alloy as well. Kruger *et al.* [41] also reported that water quenching led to higher hardness values due to a much higher dislocation density and sometimes twins in Ti-6Al-4V alloy. A similar phenomenon was observed by Praveen *et al.* [53] in Ni-based superalloy IN718. It is seen in Figure 4.12 that the work hardening rate was low in the as-received and FC conditions, and the work hardening rate of the AC condition lay in-between those of the WQ and the as-received/FC conditions, due to the difference in the microstructures shown in Figure 4.1.

4.4 Strain rate sensitivity

Figure 4.13 demonstrates the curves of ln(σ) vs. ln(strain rate) at different true strain values in the AC + AG condition, where the slope indicates the strain rate sensitivity, m, in the common approach as expressed by equation (4.1) [45,54]. The obtained strain rate sensitivity is shown in Table 4.1. It is seen that the strain rate sensitivity decreased with increasing true strain. Similar results were also reported by Lin and Chen [55]. However, the strain rate sensitivity values evaluated using the common approach were small. The Lindholm approach [56] was thus used to evaluate the strain rate sensitivity based on the following equation,

$$\sigma = \sigma_{10}(\varepsilon) + \sigma_1(\varepsilon)\log\dot{\varepsilon}\,. \qquad (4.6)$$

The Lindholm strain-rate sensitivity, m_L, is the slope, $\sigma_1(\varepsilon)$, of σ vs. $\log\dot{\varepsilon}$ based on the above equation. A typical plot of σ vs. $\log_{10}\dot{\varepsilon}$ at different true strain values is shown in Figure 4.14,

and the evaluated m_L [or $\sigma_1(\varepsilon)$] is also given in Table 4.1. Again, the strain rate sensitivity decreased as the true strain increased. The Lindholm strain-rate sensitivity values are much larger than the strain-rate sensitivity values evaluated via the common approach. However, both the common and Lindholm strain rate sensitivity values decreased monotonically with increasing true strain. Similar results were also reported in non-ELI grade of Ti-6Al-4V [48], extruded AZ31 magnesium alloy [55] and ultrafine-crystalline Cu [57].

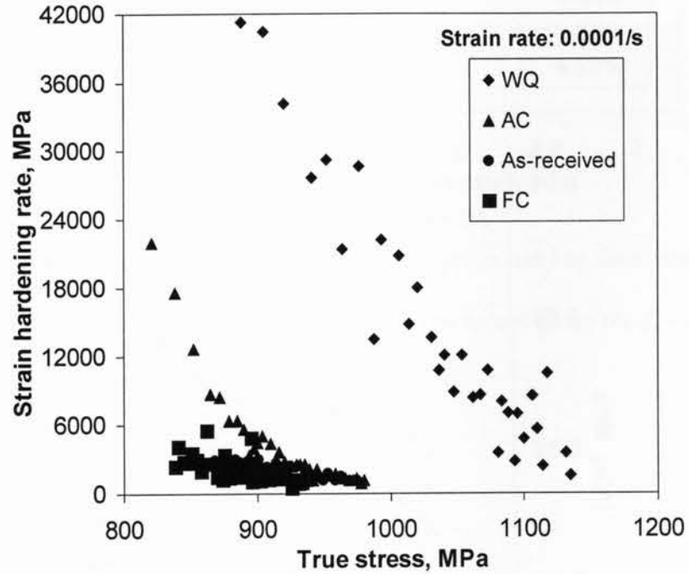

Figure 4.12 Strain hardening rate versus true stress for the Ti-6Al-4V ELI alloy in different conditions tested at a strain rate of 0.0001 s^{-1}.

Table 4.1 *Strain-rate sensitivity values for the air cooling (AC) specimens, evaluated via the common approach (m) and Lindholm approach (m_L).*

True strain, %	m	m_L
1.5	0.0139	30.22
2.0	0.0134	29.58
2.5	0.0126	28.14
3.0	0.0120	27.11

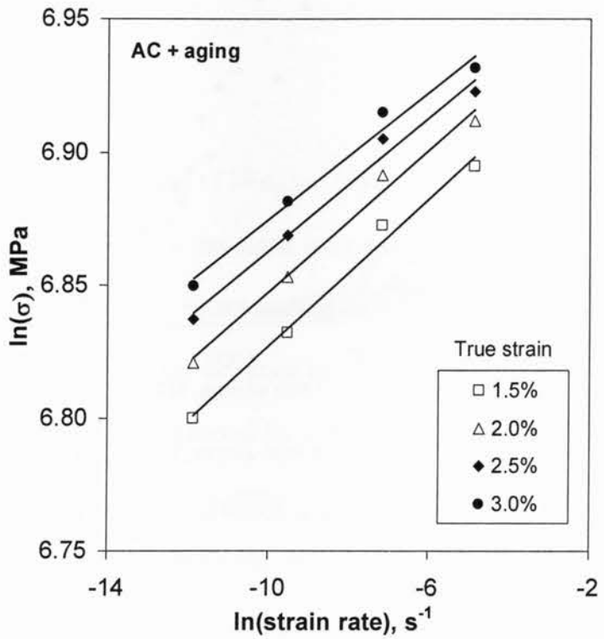

Figure 4.13 *A typical plot of ln(true stress) versus ln(strain rate) to evaluate the strain rate sensitivity, m, at different true strain values using the common approach for the AC+aging specimens.*

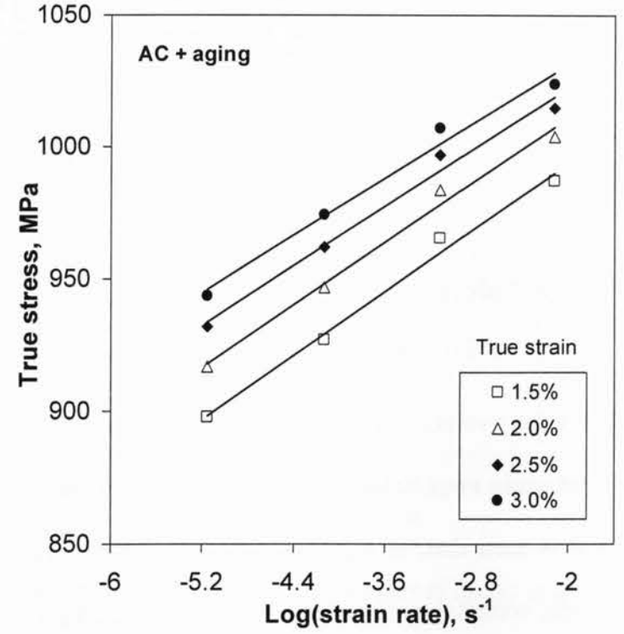

Figure 4.14 *A typical plot of true stress versus $\log_{10}$(strain rate) to determine the strain rate sensitivity, m_L, at different true strain values using the Lindholm approach for the AC+aging specimens.*

CHAPTER FIVE

Low Cycle Fatigue Behavior

5.1 Stress amplitude

Figure 5.1 shows the evolution of cyclic stress amplitude with respect to the number of cycles at different strain amplitudes on a semi-log scale for the Ti-6Al-4V ELI alloy in the AC condition. It is seen that, at high strain amplitudes (0.6 and 0.8 %) the AC sample showed slight cyclic softening until failure, with the curve of the 0.8% strain amplitude being a bit steeper than that of the 0.6% strain amplitude. Similar cyclic softening throughout the fatigue lifetime at a high strain amplitude of 1.1% was presented by Kennedy [58]. At lower strain amplitudes of 0.2%, 0.3% and 0.4%, the stress amplitude remained constant and thus no cyclic hardening or softening effect occurred. It is also seen that stress amplitudes increased with increasing total strain amplitude. Similar results were observed in the FC and as-received materials. However, the cyclic stress amplitude was the highest for the AC specimen, in the middle for the as-received specimen, and the lowest for the FC specimen, as shown in Figure 5.2. This would be associated with the microstructure (Figure 4.1) and the relevant microhardness (Figure 4.2). Similar results were reported by Srivatsan *et al.* for Ti-6Al-4V/TiB composite specimens tested at room temperature [59]. Kennedy [58] also reported that the harder material showed a higher stress amplitude value for non-ELI Ti-6Al-4V alloy.

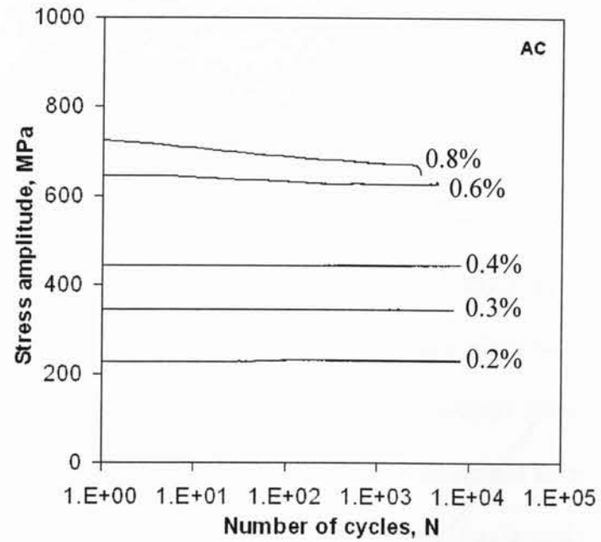

Figure 5.1 *Stress amplitude as a function of the number of cycles at different total strain amplitudes for the AC condition.*

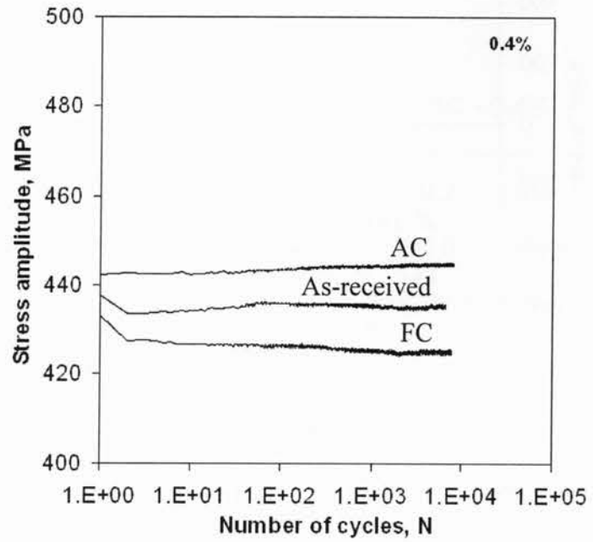

Figure 5.2 *Stress amplitude as a function of the number of cycles at a strain amplitude of 0.4% for three material conditions.*

5.2 Hysteresis loops and mean stress change

Typical hysteresis loops for strain amplitudes of 0.4%, 0.6% and 0.8% for AC samples at the half-life cycles are shown in Figure 5.3. At a strain amplitude of 0.4% or below, no plastic deformation was seen. Even at the strain amplitude of 0.6%, only a small plastic strain range was observed. At the strain amplitude of 0.8%, the plastic strain range became larger, but a somewhat asymmetric hysteresis loop was seen. This may be due to the twinning in the compressive phase of the cyclic deformation, like the hysteresis loops of magnesium alloys, which also have a hexagonal close-packed crystal structure [60,61].

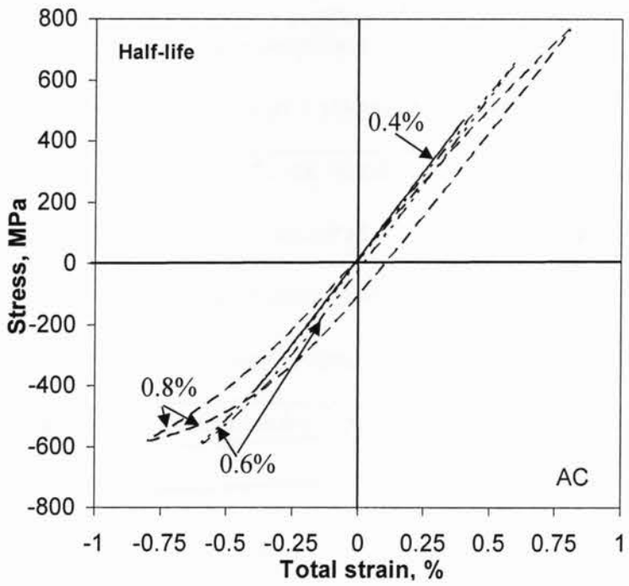

Figure 5.3 *Typical stress-strain hysteresis loops of AC sample at the half-life at a total strain amplitude of 0.4%, 0.6% and 0.8%.*

Figure 5.4 and 5.5 show a few typical stress-strain hysteresis loops for the AC sample at total strain amplitudes of 0.4% and 0.8%. It is seen from Figure 5.4 that, at a strain amplitude of 0.4%, the hysteresis loops did not change much in the entire fatigue process, thus no cyclic hardening/softening occurred. Similar results were reported by Wang *et al.* [62] for a composite containing Ti_3Al phase.

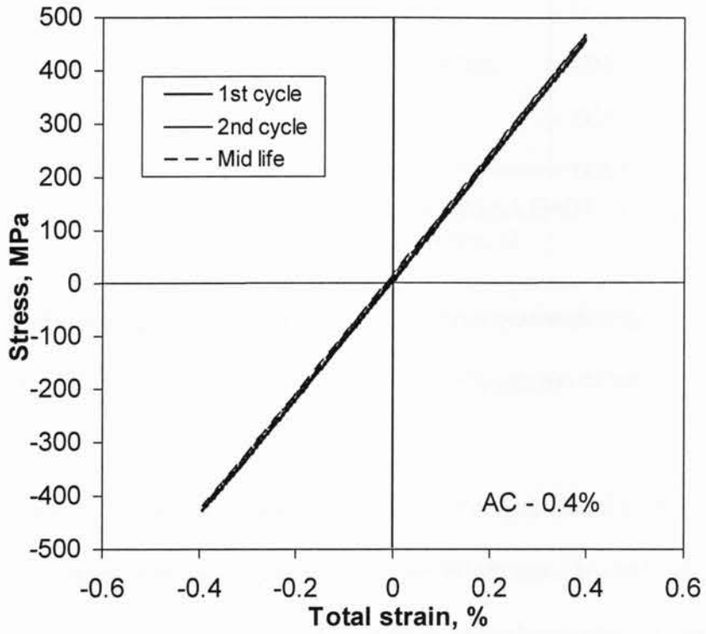

Figure 5.4 *Typical stress-strain hysteresis loops of different cycles for the AC sample at a total strain amplitude of 0.4%.*

At the higher strain amplitude of 0.8% (Figure 5.5), the difference between the initial cycles and the mid-life cycle hysteresis loops was observed, exhibiting the strain softening effect, which can also be seen in Figure 5.1. This was also similar to the result obtained at higher strain amplitudes by Wang *et al.* [62] for a precipitate-free Ti composite.

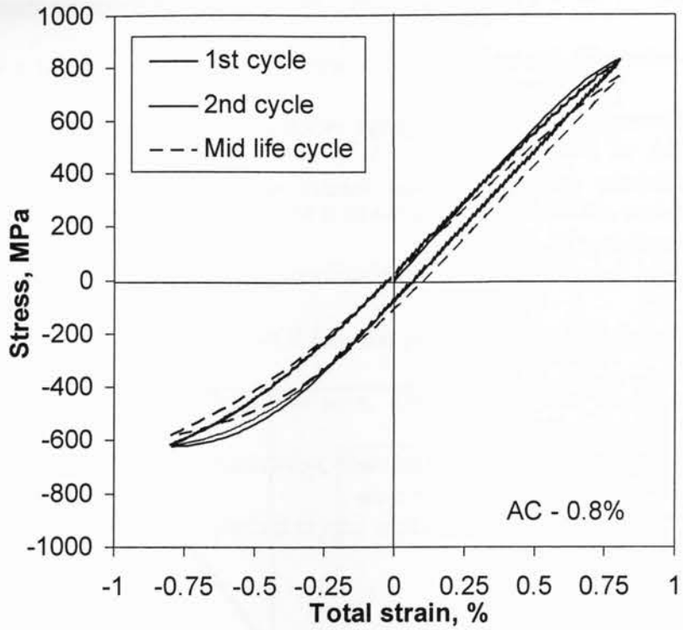

Figure 5.5 *Typical stress-strain hysteresis loops of different cycles for the AC sample at a total strain amplitude of 0.8%.*

The mean stress plotted as a function of the number of cycles at different applied strain amplitudes for the AC sample is shown in Figure 5.6. The mean stress increased with increasing total strain amplitudes, which is also in agreement with the result reported in [63,64]. At the higher strain amplitude (0.8%), the mean stress decreased until failure, and it remained nearly constant throughout the entire fatigue life at the strain amplitude of 0.6%. At the lower strain amplitudes (0.2% and 0.4%), the mean stress slightly increased up to about 100 cycles and then became constant.

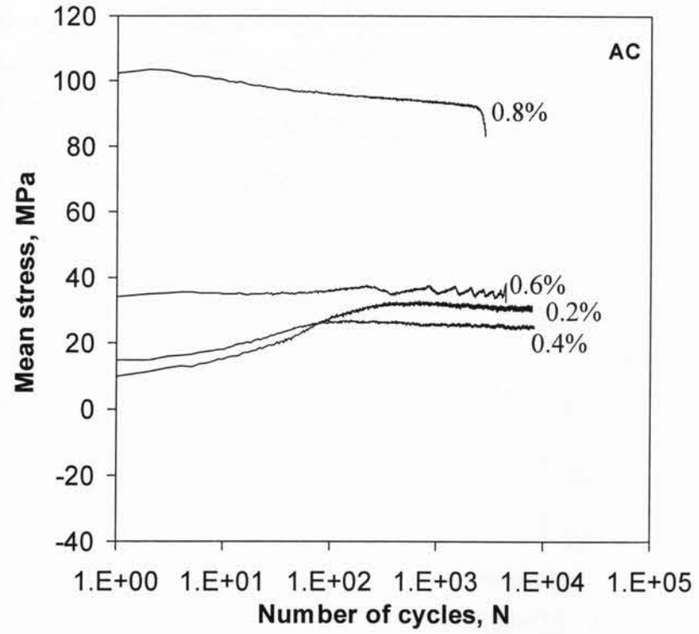

Figure 5.6 *Variation of mean stress with the number of cycles at different total strain amplitudes for the AC material.*

Figure 5.7 shows the variation of mean stress at a strain amplitude of 0.4% with the number of cycles for the three material conditions. After the initial change within about 100 cycles, the mean stress remained almost constant, being the highest for the AC sample, followed by the as-received and the FC samples.

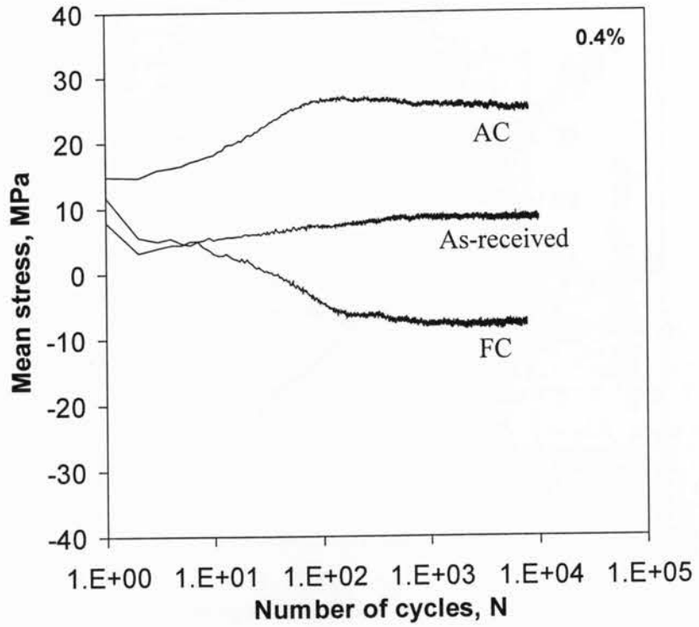

Figure 5.7 *Variation of mean stress with the number of cycles at a strain amplitude of 0.4% for three material conditions.*

5.3 Fatigue life

Figure 5.8 shows the strain-life diagram of the Ti-6Al-4V ELI alloy in the three material conditions. As the applied total strain amplitude decreased, the number of cycles to failure increased. The fatigue life was slightly lower in the AC or FC conditions, especially at the lower strain amplitudes, in spite of the presence of experimental scatter.

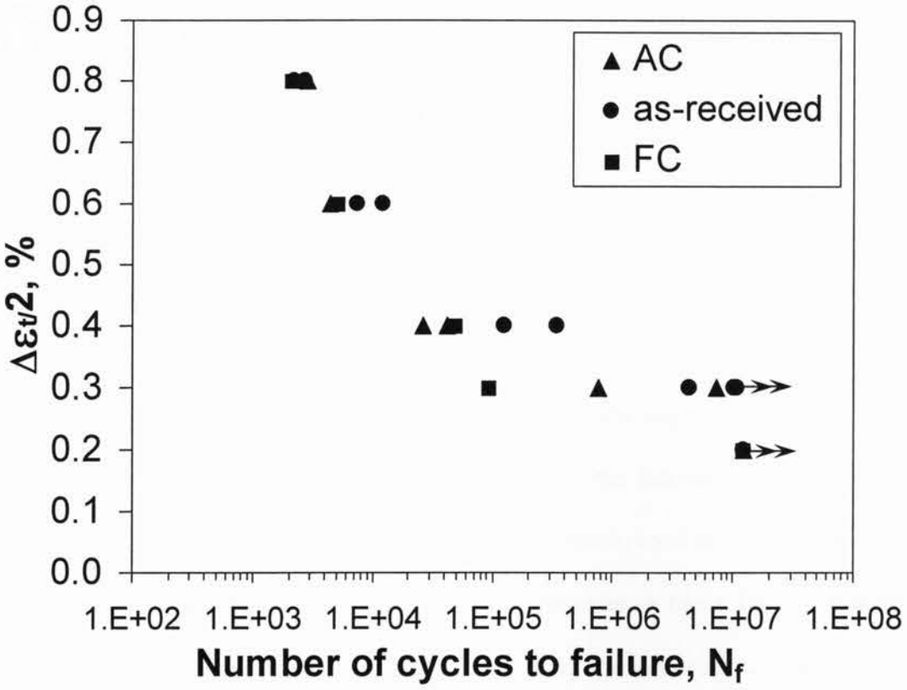

Figure 5.8 *Effect of the total strain amplitude on fatigue lifetime of the Ti-6Al-4V ELI alloy in the three material conditions.*

The results obtained in the as-received and AC conditions were similar to those obtained by Turner [65] for the heat treated Ti-6Al-4V ELI alloy, who reported that fatigue life degraded with increasing α platelet size. This could be seen in Figure 4.1(a) and (c). However, the FC condition showed the lowest fatigue life due to the presence of the large equiaxed α microstructure. Eylon and Pierce [66], in their study on the effect of notch fatigue properties of the Ti-6Al-4V alloy, observed that, at low stress levels, the nucleated crack was limited in size to the width of a single α needle, while at high stresses, the nucleated crack may be as large as the entire colony of similarly aligned α needles. Shizawa *et al.* [67], after conducting

low cycle fatigue tests for the Ti-6Al-4V alloy at elevated temperatures, also observed the highest low-cycle fatigue strength for the bi-modal microstructure followed by the equiaxed α structure.

CHAPTER SIX

Fractals and Fractography

6.1 Introduction to fractal analysis in materials science

Materials science is one of the fields in which quantitative fractography is critical since the mechanical properties of materials are directly related to the fracture mode/mechanism or microscopic fracture events. The concept of fractal dimension, used to describe the irregular surfaces with a self-similar (or self-affine) nature, provides a basis for the quantitative characterization of the tortuosity of fracture surfaces, and the potential linkage between the fractal dimension and mechanical properties. Manderbrot *et al.* [68,69] first introduced this concept to materials science in 1984. Since then, considerable work has been reported in the literature. The fractal dimension has recently been used to estimate the theoretical strength of materials [70], analyze the well-known experimental findings on the size effect of fatigue strength of materials [71], model the dominating damage mechanism in ductile fracture [72], and offer a new theoretical basis for the empirical Kitagawa diagram used to describe the variation of the fatigue threshold stress intensity range with the crack length [73]. Fractal geometry, fracture mechanics, molecular dynamics and molecular orbital calculations, and fractographic observations have also been used jointly to link the atomic bond-breaking process to the formation of the observed fracture surface topography [74].

6.1.1 Contradictory relationships

Different relationships between the fractal dimension of fracture surfaces and mechanical properties have been reported in the literature. Hilders *et al.* [75,76] reported that yield strength and ultimate tensile strength (UTS) decreased and impact energy/toughness increased with increasing fractal dimension for duplex stainless steel tested at room temperature. Dai and Wu [77] reported that the fractal dimension increased with increasing toughness in a composite material. Hsiung and Chou [78] observed that the fractal dimension increased with increasing impact toughness in a high strength low alloy steel. Wang *et al.* [77] reported that the fatigue threshold of a dual-phase steel increased with increasing fractal dimension. These results indicated that the higher the fractal dimension value, the rougher the surface and the tougher the material [79].

On the other hand, Manderbrot *et al.* [68] reported that the impact energy decreased as the fractal dimension increased for a 300-grade maraging steel after Charpy impact tests. Richards and Dempsey [81] observed similar results, i.e., a slight increase of UTS with increasing fractal dimension in Ti-4.5Al-5.0Mo-1.5Cr alloy. Pande *et al.* [82] also reported a negative relationship between the dynamic tear energy and the fractal dimension of fracture surfaces in the Ti-6Al-2V alloy with varying amounts of Zr.

6.1.2 Methods of measuring fractals

These different relationships have been pointed out to be associated with the measurement methods [83-89]. A number of methods used to determine the fractal dimension of fracture surfaces have been reported, including the slit island method [68,79,82,90], the vertical section method [82,91], the secondary electron line scanning method [89]. Manderbrot *et al.* [68] first used the slit island method, where a certain amount of peaks on the fracture surface were ground off and polished. This procedure generated the so-called "islands and lakes" pattern on the fracture surface. The fractal dimension was then determined on the basis of the perimeter as a function of the area of either “island” or “lakes” [68,92]. Drury and Gokhale [86] used the profilometry data to measure the fractal dimensions by defining a surface roughness parameter as the ratio of total apparent surface area to the projected area, which basically became a three-dimensional (3D) analogue to profile roughness. To overcome the difficulties of one- and two-dimensional measurements [68,82,90,91], fractal analysis has been conducted using 3D topography of fracture surfaces by reconstructing and quantifying by means of SEM stereo pairs, image processing and analysis and computer vision [93-97]. It appeared that the method related to the 3D area measurements of irregular fracture surfaces with varying scale lengths would be more appropriate to determine the fractal dimension of fracture surfaces. The objective of this investigation was, therefore, to determine the fractal dimension of fracture surfaces of the Ti-6Al-4V ELI alloy via 3D measurements of fracture surface areas, and identify the relationship between the fractal dimension and the mechanical properties.

6.2 Three-dimensional fractal measurement

In the Area-Scale Analysis, to measure the fractal dimension. the following equation is used [97],

$$R_s = R_o r^{(2-D_f)}, \tag{6.1}$$

where R_s is the measured relative area, r is the linear scale (i.e., the side length of equilateral triangles in μm or nm), R_o is a constant, D_f is the fractal dimension. Taking logarithms in Equation 6.1,

$$\log R_s = \log R_o + (2 - D_f)\log r, \tag{6.2}$$

Therefore,

$$D_f = 2 - slope, \tag{6.3}$$

in the logR_s versus log$r$ graph.

Fractal dimensions were determined via three-dimensional (3D) measurements of fracture surfaces areas versus the ruler scale (i.e., the side length of equilateral triangular tiles) using MeX software. The images of fracture surfaces used for the fractal analysis were taken near the centre and joined to form a 3D image at a magnification of 1000 times. Three 3D images were analyzed for each material condition after converting them into a digital elevation model (DEM) using a cut-off wavelength of 15λ, where λ is in micrometers. A typical example is shown in Figure 6.1, where the relative area (the ratio of the measured 3D fracture surface area to its projected area) is plotted as a function of the ruler scale (or lateral resolution) in double-log coordinates.

The fractal dimension of the fracture surface is evaluated from the slope, k, of the dashed line fitted through the linear portion of data points (Figure 6.1) via equation (6.3),

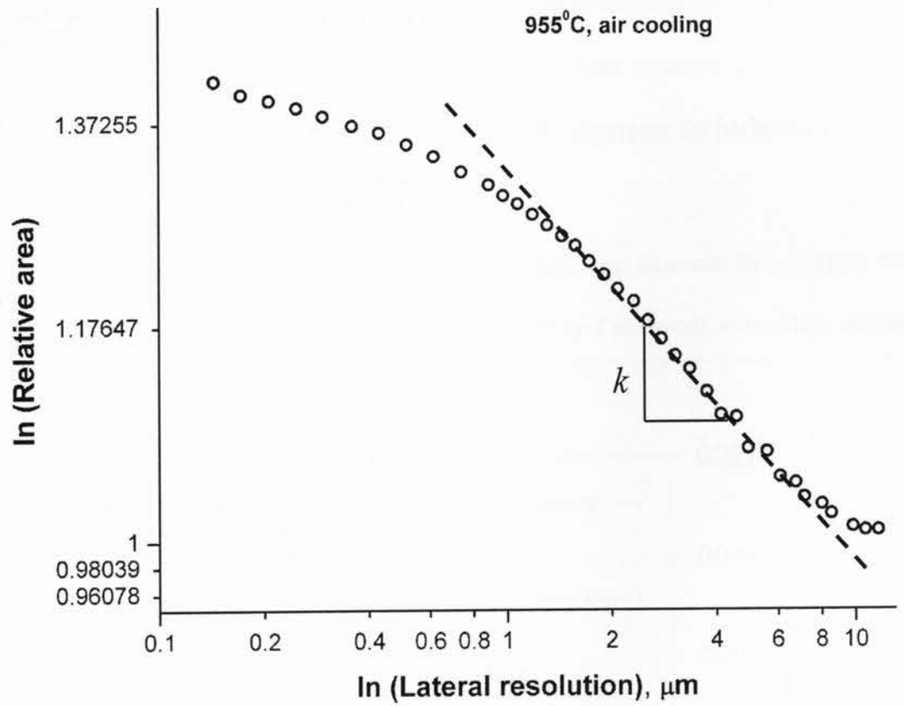

Figure 6.1 *A typical plot of the relative area versus the lateral resolution (ruler scale) in a double-log coordinate for the specimen subjected to heat treatment at 955 ℃ and air cooling.*

The average surface roughness, S_a, defined as [97],

$$S_a = \frac{\iint |Z(x,y)| dxdy}{A_e}, \qquad (6.4)$$

was evaluated from the 3D images of fracture surfaces, where $Z(x,y)$ is the height function representing the point-by-point deviations between the measured topography and the mean surface, and A_e is the evaluation area.

6.3 Variation of strength, ductility and roughness with the fractal dimension

The variation of strength and ductility of Ti-6Al-4V ELI alloy with fractal dimension of fracture surfaces is shown in Figure 6.2 and Figure 6.3.

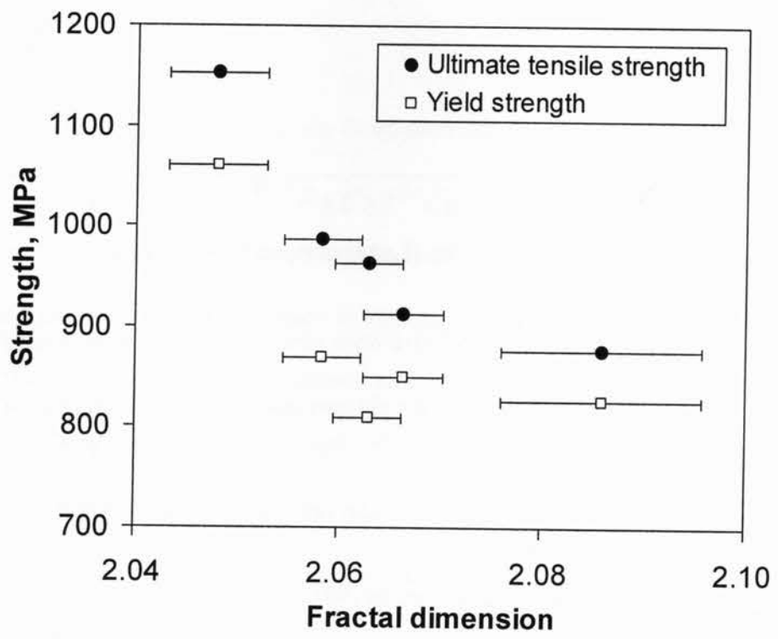

Figure 6.2 *Variation of yield strength and ultimate tensile strength, with fractal dimension of fracture surfaces in Ti-6Al-4V ELI alloy.*

It is seen that both the yield strength (YS) and ultimate tensile strength (UTS) decreased, while the ductility (as indicated by the percent elongation) increased with increasing fractal dimension (D_f). Similar results on 7075-T651 aluminum alloy were reported by Hilders *et al.* [98]. It is seen from Figure 6.3 that the more ductile specimens, corresponding to lower strengths arising from varying heat-treatment conditions, were represented by higher values of fractal dimension. This is in agreement with the results reported in the literature: the rougher the fracture surfaces, the larger the fractal dimension [68,75-80,98].

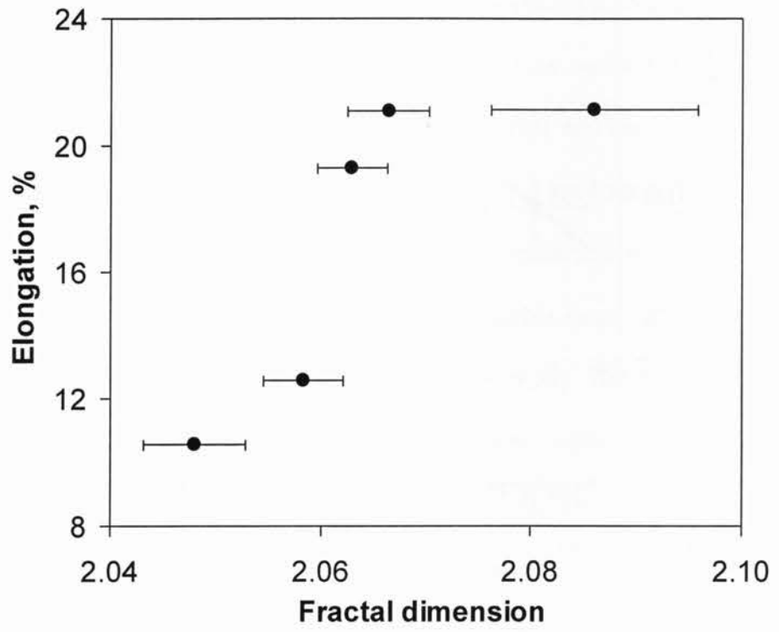

Figure 6.3 *Variation of ductility, with fractal dimension of fracture surfaces in Ti-6Al-4V ELI alloy.*

This is further corroborated by direct 3D measurements of the average roughness S_a values obtained from the fracture surfaces in different heat treatment conditions as shown in Figure

6.4. The fractal dimension increased linearly with increasing roughness, which could be described by the following equation,

$$D_f = 0.071 S_a + 1.99. \quad (6.5)$$

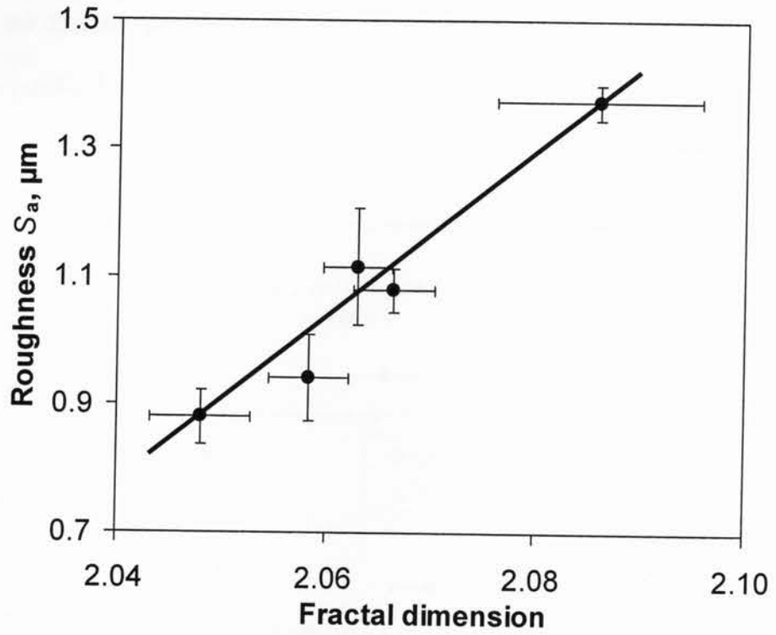

Figure 6.4 *Average roughness S_a versus fractal dimension of fracture surfaces in Ti-6Al-4V ELI alloy.*

The roughness of fracture surfaces is basically associated with the fracture mode or mechanism, which is in turn dependent on the microstructures or heat treatment conditions. In general, the mode of ductile fracture gives rise to a rougher fracture surface, coupled with more energy absorption during the fracture process, whereas the brittle fracture or cleavage fracture (e.g., the fracture of glasses) is flatter. Typical fracture surfaces of the Ti-6Al-4V

ELI alloy studied are shown in Figure 6.5 in both as-received (Figure 6.5(a)) and heat-treated (Figure 6.5(b,c,d,e,f)) conditions. As seen from Figure 6.5(a), the as-received material exhibited a characteristic dimple-like ductile fracture with a large number of tear ridges. While the fracture surface after furnace cooling (representing the softest material state) exhibited a similar dimple-like ductile fracture, the tear ridges appeared to be more pronounced or higher, as seen in Figure 6.5(b). Compared to the furnace-cooled specimen, the air cooling seemed to cause a lesser degree of tear ridges, Figure 6.5(c), although the fracture mode for both furnace cooling and air cooling still exhibited a ductile with the dimpled rupture. The fracture surface of the air-cooled specimen after aging, Figure 6.5(d), consisted of dimples with some cleavage-like facets, and the surface roughness was visibly less when compared to the furnace-cooled (Figure 6.5(b)) and air-cooled (Figure 6.5(c)) specimens. In the water-quenched and water-quenched plus aged specimens, Figure 6.5(e,f), the fracture mode was more of cleavage cracking in conjunction with some dimples, thus resulting in a lower surface roughness compared to all other cases. This is attributed to the presence of martensite arising from the water quench [99,39]. The observed fracture mode corresponded well to the measured values of fracture surface roughness and fractal dimension, as presented in Figure 6.4 or Equation (6.4). These 3D measurements thus revealed that the fractal dimension was a measure of fracture surface roughness. As a result, the variation of the strength and ductility with fractal dimension (Figure 6.2) was primarily attributed to the variation of the fracture surface roughness or fracture mode, caused by varying heat treatment conditions.

6.4 Examination of fatigue fracture surfaces

Figure 6.6 shows a few typical SEM images of fracture surfaces of the AC condition after fatigue tests. From the low-magnification SEM images showing the overall view of the fracture surfaces at the total strain amplitude of 0.4% and 0.8%, Figure 6.6(a)-(c), it is seen that fatigue crack initiation in all the tested specimens, regardless of the applied strain amplitudes, occurred from the specimen surface. However, at the higher strain amplitude of 0.8%, multiple crack initiation was observed, as indicated by the dashed lines in Figure 6.6(b). In another AC sample tested at a strain amplitude of 0.4%, the initiation site and propagation zone could be clearly seen at a slightly higher magnification (Figure 6.6(c)). Fatigue crack propagation was characterized by the characteristic fatigue striations, in conjunction with some secondary cracks and tear ridges, as shown in Figure 6.6(d).

Figure 6.7 shows typical SEM images of fracture surfaces of the Ti-6Al-4V ELI alloy in the FC condition fatigued at a total strain amplitude of 0.4%. Again, the crack initiated from the specimen surface (Figure 6.7(a)). A close examination at higher magnification indicated that the crack initiation site had quasi-cleavage features, coupled with slip band cracking in some grains and secondary cracks. Also, the plastic deformation marks could clearly be seen. Fatigue crack propagation was again characterized by the typical fatigue striations, coupled with some secondary cracks and tear ridges, as shown in Figure 6.7(c) and (d). With increasing distance from the crack initiation site, the spacing of the fatigue striations increased.

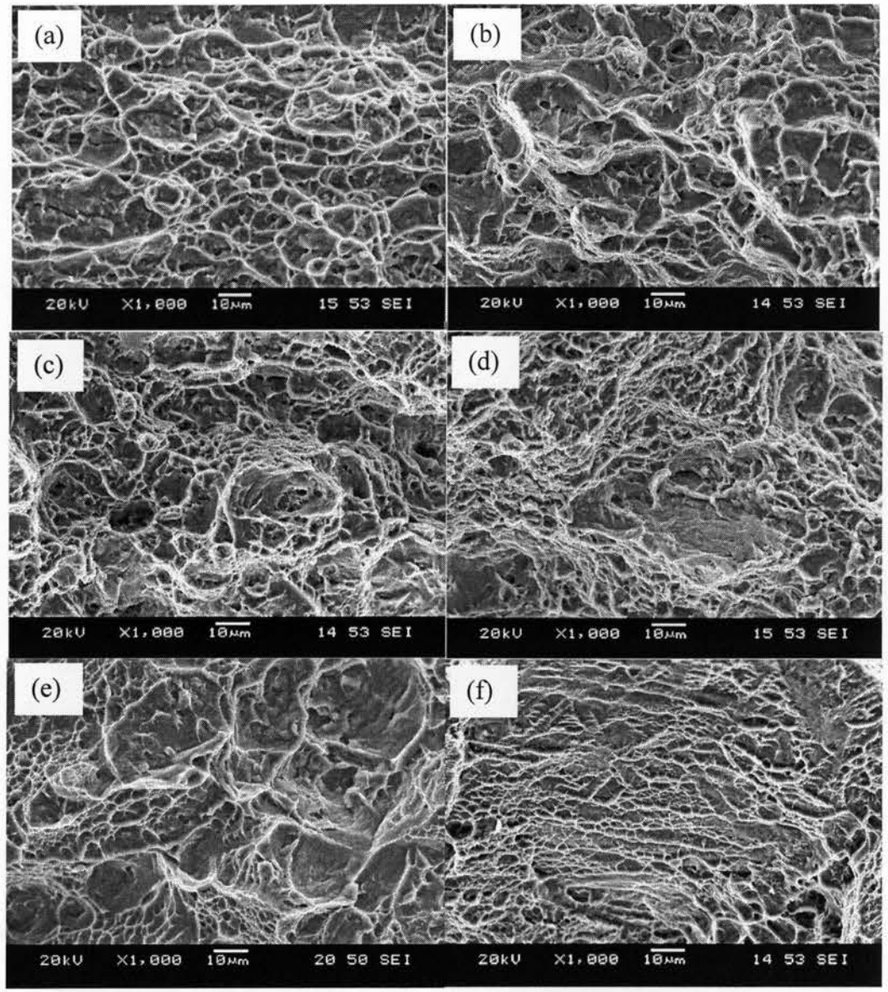

Figure 6.5 SEM micrographs of the test specimens in different conditions, (a) as-received, (b) furnace cooling, (c) air cooling, (d) air cooling plus aging, (e) water quenching and (f) water quenching plus aging.

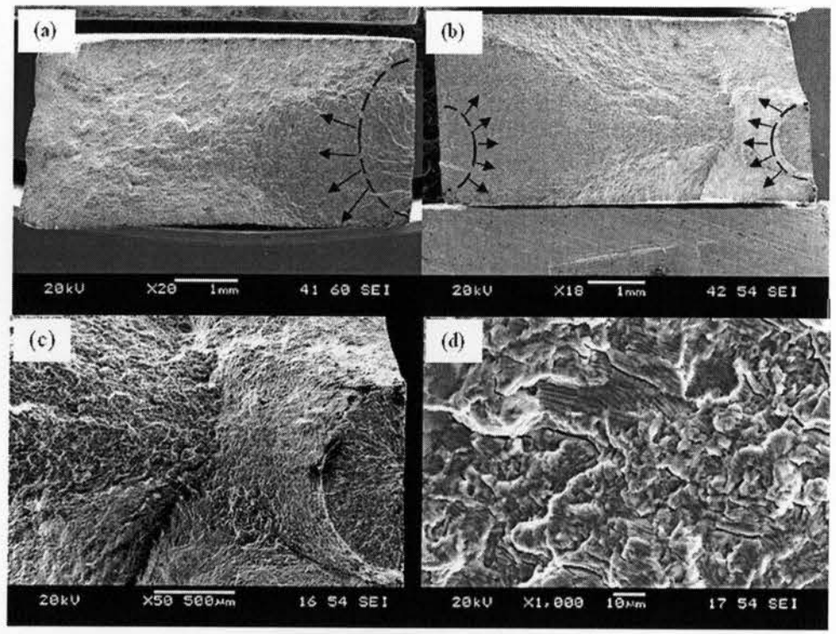

Figure 6.6 *Typical SEM micrographs of the Ti-6Al-4V ELI alloy in the AC condition after low cycle fatigue tests. (a) low-magnification SEM images showing the overall view of the fracture surface at a total strain amplitude of 0.4%, (b) low-magnification SEM images showing the overall view of the fracture surface at a total strain amplitude of 0.8%, (c) SEM image showing the overall view of the fracture surface at a total strain amplitude of 0.4% for another AC sample at a higher magnification, (d) SEM image at higher magnification showing the crack propagation zone.*

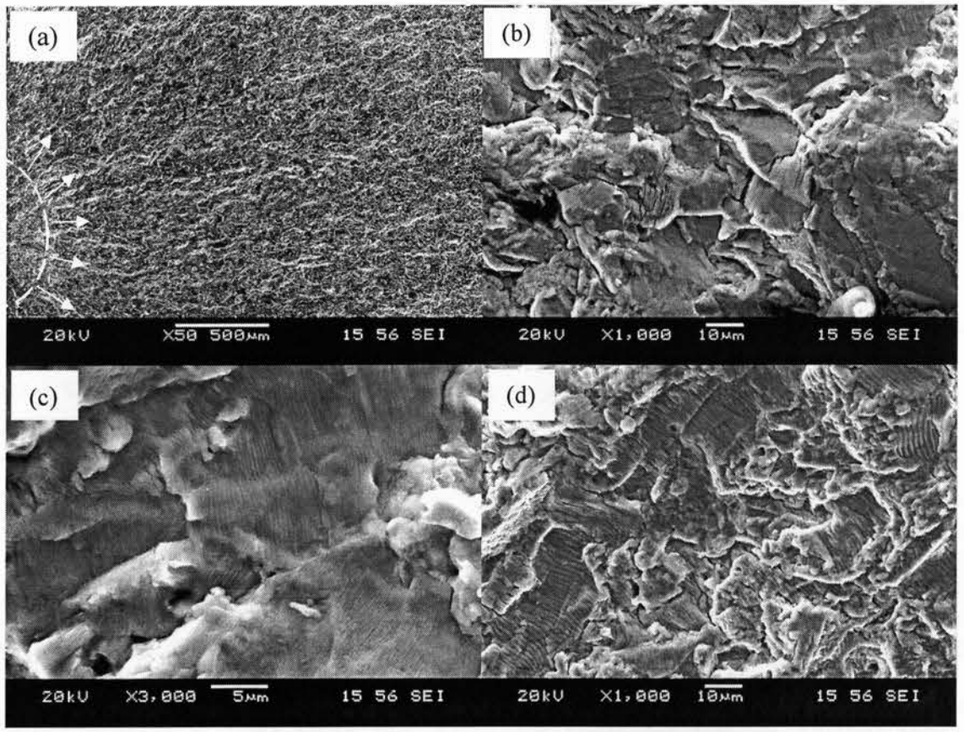

Figure 6.7 *Typical SEM micrographs of the Ti-6Al-4V ELI alloy in the FC condition fatigued at a total strain amplitude of 0.4%. (a) low-magnification SEM image showing the crack initiation site at the specimen surface. (b) SEM image at a higher magnification showing the crack initiation area near the specimen surface, (c) SEM image showing the crack propagation area close to the initiation site. (d) SEM image showing the crack propagation zone at a higher magnification.*

CHAPTER SEVEN

Conclusions and Future Work

7.1 Conclusions

1. The as-received Ti-6Al-4V ELI alloy consisted of primary α and α+β phases. Furnace cooling (FC) from 955°C led to a microstructure of equiaxed α and intergranular β; air cooling (AC) and air cooling plus aging (AC + aging) resulted in a microstructure of acicular α and β plus primary α; the microstructure after water quenching (WQ) consisted of α'+β plus primary α; and the water quenching and aging (WQ + aging) resulted in a microstructure of primary α and α'+β plus some fine secondary α phase in the β phase.

2. The heat treatments led to effective surface hardening due to the formation of a thermal oxidation layer of about 0.15 mm depth. While the AC slightly increased the interior hardness, the WQ significantly increased the internal hardness due to the formation of martensite. The lowest interior hardness was observed in the FC condition, mainly due to the equiaxed α.

3. The hardened surface layer seemed to have a minor effect on the yield strength (YS) and led to a small decrease in the ultimate tensile strength (UTS), and some reduction in the ductility was observed.

4. The YS and UTS were the highest for the WQ + aging specimen and the lowest for the FC specimen. The WQ condition basically showed the next highest UTS values, followed by AC + aging and AC conditions. While the UTS of the as-received specimen lay in-between that of the AC and FC specimens, it had the highest ductility.

5. Both YS and UTS increased, and the ductility decreased with increasing strain rate for all material conditions.

6. The strain hardening exponent evaluated based on the Hollomon equation was observed to decrease as the strain rate increased. The as-received material exhibited a higher strain hardening exponent evaluated based on the Ludwig and modified methods followed by FC, AC and WQ. The Ludwig and modified methods gave higher values of the strain hardening exponent.

7. The strain hardening rate (from high to low) was observed to be just the reverse from WQ, AC, FC to the as-received condition. The harder materials showed a higher initial work hardening rate due to a higher dislocation density and sometimes twins.

8. The strain rate sensitivity evaluated using both the common approach and the Lindholm approach was found to decrease with increasing true strain, although the Lindholm strain-rate sensitivity values were much larger than those evaluated using the common approach.

9. Both stress amplitude and mean stress increased with increasing total strain amplitude. Cyclic softening was observed at higher total strain amplitudes (0.6-0.8%), while the stress amplitude remained nearly constant at lower total strain amplitudes (0.2-0.4%). At the higher strain amplitude of 0.8%, asymmetric hysteresis loops were also observed.

10. Both stress amplitude and mean stress were higher for the AC sample when compared to the FC sample, the as-received sample fell in-between the AC and FC conditions.

11. Fractal dimension of the tensile fracture surfaces was found to be the highest in the FC condition, corresponding to the highest ductility. The fractal dimension increased as the roughness of fracture surfaces increased.

12. After tensile tests, the as-received and FC materials exhibited a characteristic dimple-like ductile fracture with a large number of tear ridges. The fracture surface of the AC + aging and AC specimen consisted of dimples with some cleavage-like facets. The fracture mode in the WQ + aging and WQ conditions exhibited more of cleavage cracking in conjunction with some dimples.

13. Fatigue crack initiation was observed to occur at the specimen surface, regardless of the applied strain amplitudes and heat treatment conditions. At the higher strain amplitude, multiple crack initiation occurred. Fatigue crack propagation was characterized by the characteristic fatigue striations, coupled with some secondary cracks and tear ridges

7.2 Recommendations for future work

1. This work dealt with the heat treatment of Ti-6Al-4V ELI alloy below the transus temperature of 975°C. Studies are needed to understand the microstructure and properties of this alloy slightly above the transus temperature.

2. Detailed thermal oxidation heat treatment (HT) and microstructural characterization via changing HT parameters are of interest.

3. Stress-controlled high cycle fatigue tests are needed to examine the effect of thermal oxide hardened layer on fatigue life.

4. The effect of the thermal oxide hardened layer on the fatigue crack propagation behavior is also important.

References

[1] H.J. Rack and J.I. Qazi, Titanium alloys for biomedical applications, *Materials Science and Engineering C*, 2006, 26(8), 1269-1277.

[2] G. He and M. Hagiwara, Ti alloy design strategy for biomedical applications, *Materials Science and Engineering C*, 2006, 26, 14 -19.

[3] M.D. Naughton and P. Tiernan, Mechanical behaviour and superplastic forming capabilities of extra-low interstitial grade Ti-6Al-4V wire alloy with numerical verification, *Proceedings of the Institution of Mechanical Engineers, Part L: Journal of Materials*, 2007, 221, 165-174.

[4] R.T. Bothe, L.E. Beaton and H.A. Davenport, Reactions of bone to multiple metallic implants, *Surgery, gynecology & obstetrics*, 1940, 71, 598-602.

[5] G.S. Leventhal, Titanium, a metal for surgery, *The Journal of bone and joint surgery*, 1951, 33-A(2), 473-474.

[6] K. Wang, The use of titanium for medical applications in the USA, *Materials Science and Engineering A*, 1996, 213, 134-137.

[7]. W.H. Lee and C.Y. Hyun, Fabrication of fully porous and porous-surfaced Ti-6Al-4V implants by electro-discharge-sintering of spherical Ti-6Al-4V powders in an one-step process, *Journal of Materials Processing Technology*, 2007, 189(1-3), 219-223.

[8] M. Long and H.J. Rack, Titanium alloys in total joint replacement-a materials science perspective, *Biomaterials,* 1998, 19, 1621-1639.

[9] M. Niinomi, Recent metallic materials for biomedical applications, *Metallurgical Materials Transactions*, 2002, 33A, 477-486.

[10] M. Niinomi, Mechanical properties of biomedical titanium alloys, *Materials Science & Engineering A, 1998,* 243, 231-236.

[11] B M. Balazic, J. Kopac, M.J. Jackson and W. Ahmed, Review: titanium and titanium alloy applications in medicine, *International Journal of Nano and Biomaterials*, 2007, 1(1), 3-34.

[12] www.biomet.com *(http://www.biomet.com/patients/vanguard_complete.cfm)*

[13] R.O. Ritchie, J.H. Kinney, J.J. Kruzic and R.K. Nalla, A fracture mechanics and mechanistic approach to the failure of cortical bone, *Fatigue & Fracture of Engineering Materials & Structures*, 2005, 28, 345-371.

[14] S.H. Teoh, Fatigue of biomaterials: A review, *International Journal of Fatigue*, 2000, 22, 825–837.

[15] T. Akahori and M. Niinomi, Fracture characteristics of fatigued Ti-6Al-4V ELI as an implant material, *Materials Science and Engineering A*, 1998, 243, 237-243.

[16] E.A. Magnissalis, S. Zinelis, G. Hartofilakidis and T. Karachalioset, Failure Analysis of Two Ti-Alloy Total Hip Arthroplasty Femoral Stems Fractured In Vivo, *Journal of Biomedical Materials Research - Part B Applied Biomaterials*, 2003, 66(1), 299-305.

[17] S. Griza, C. Kwietniewski, G.A. Tarnowski, F. Bertoni, Y. Reboh, T.R. Strohaecker and I.J.R.Baumvol, Fatigue failure analysis of a specific total hip prosthesis stem design, *International Journal of Fatigue,* 2008, 30(8), 1325-1332.

[18] Fragomeni, J.M., Effect of heat treating on the microstructure and fatigue behavior of a Ti-6Al-4V ELI alloy, *Journal of Advanced Materials*, 2001, 33, 18-25.

[19] C. Leinenbach, and D. Eifler, Fatigue and cyclic deformation behaviour of surface-modified titanium alloys in simulated physiological media, *Biomaterials*, 2006, 27(8), 1200-1208.

[20] C. Leinenbach, B. Schwilling, and D. Eifler, Cyclic deformation behaviour and fatigue induced surface damage of titanium alloys in simulated physiological media, *Materials Science and Engineering C*, 2005, 25 (3), 321-329.

[21] H. Guleryuz and H. Cimenoglu, Surface modification of a Ti-6Al-4V alloy by thermal oxidation, *Surface and Coatings Technology*, 2005, 192, 164-170.

[22] A. Biswas, L. Li, U.K. Chatterjee, I. Manna, S.K. Pabi and J.M. Dutta, Mechanical and electrochemical properties of laser surface nitrided Ti-6Al-4V, *Scripta Materialia*, 2008, 59, 239-242.

[23] T. Bacci, F. Borgioli and B. Tesi, Surface modification of Ti-6Al-4V alloy by means of combined plasma nitriding and oxidizing treatments, *Surface Engineering*, 1998, 14(6), 500-504.

[24] A. Biswas, U.K. Chatterjee, I. Manna, S.K. Pabi and J.M. Dutta, Surface oxidation of Ti-6Al-4V for bio-implant application, *Surface Review and Letters*, 2007, 14, 597-600.

[25] D. Velten, V. Biehl, F. Aubertin, B. Valeske, W. Possart and J. Breme, Preparation of TiO_2 layers on cp-Ti and Ti-6Al-4V by thermal and anodic oxidation and by sol–gel coating techniques and their characterisation., *Journal of Biomedical Materials Research,* 2002, 59, 18–28.

[26] M.M. Yazdanian, A. Edrisy, and A.T. Alpas, Vacuum sliding behaviour of thermally oxidized Ti-6Al-4V alloy, *Surface and Coatings Technology*, 2007, 202(4-7) , 1182-1188.

[27] P.A. Dearnley, K.L. Dahm and H. Cimenoglu, The corrosion-wear behaviour of thermally oxidised CP-Ti and Ti-6Al-4V, *Wear*, 2004, 256, 469-479.

[28] F. Borgioli, E. Galvanetto, F. Iozzelli and G. Pradelli, Improvement of wear resistance of Ti-6Al-4V alloy by means of thermal oxidation, *Materials Letters*, 2005, 59(17), 2159-2162.

[29] H. Guleryuz and H.Cimenoglu, Effect of thermal oxidation on corrosion and corrosion-wear behaviour of a Ti-6Al-4V alloy, *Biomaterials*, 2004, 25(16), 3325-3333.

[30] D. Henkel and A.W. Pense, *Structure and properties of Engineering Materials. Fifth Edition*, Mc Graw Hill publications, 2002, PP. 342-359.

[31] Properties and selection: non ferrous alloys and special purpose materials, *ASM Handbook*, 1990, 2, 10th Edition, PP. 604-605.

[32] M. Ueda, M.M. Silva, C. M. Lepienski, P.C. Soares Jr., J.A.N. Goncalves and H. Reuther, High temperature plasma immersion ion implantation of Ti-6Al-4V, *Surface and Coatings Technology*, 2007, 201, 4953-4956.

[33] M. Dudek, S. Fouvry, B. Wendler, Ph. Kaspa and T. Liskiewicz, The effect of diffusion treatment in a glow-discharge plasma in Ar + O_2 atmosphere on friction and wear of Ti-6Al-4V alloy, *Vacuum*, 2003, 70, 187-191.

[34] E. Santos Jr., N.K. Kuromoto and G.A. Soares, Mechanical properties of titania films used as biomaterials, *Materials Chemistry and Physics*, 2007, 102, 92-97.

[35] M.N. Gungor, I. Kock, L.S. Kramer, H. Dong, N.R. Martin and W.T. Tack, Microstructure and mechanical properties of highly deformed Ti-6Al-4V , *Materials Science and Engineering A*, 2005, 410-411, 369-374.

[36] W.C. Say and Y.Y. Tsai, Surface characterization of cast Ti-6Al-4V in hydrofluoric-nitric pickling solutions, *Surface and Coatings Technology*, 2004, 176, 337-343.

[37] S.L. Semiatin and T.R. Bieler, The effect of alpha platelet thickness on plastic flow during hot working of TI–6Al–4V with a transformed microstructure, *Acta Materialia*, 2001, 49(17), 3565-3573.

[38] W. Zhang, B. Wu, W.S. Zhao, D.X. Li and M.L. Sui, Formation of novel β-Ti martensites in Ti-6Al-4V under an electric-current-pulse heat treatment, *Material Science and Engineering A,* 2006, 438-440, 320-323.

[39] M.J. Donachie, Jr., *Titanium - A Technical Guide*, Second Edition, ASM International, 2000.

[40] M.T. Jovanovic, S. Tadic, S. Zec, Z. Miskovic and I. Bobic, The effect of annealing temperatures and cooling rates on microstructure and mechanical properties of investment cast Ti-6Al-4V alloy, *Materials and Design*, 2006, 27, 192-199.

[41] L. Kruger, K. Sommer, T. Halle, M. Hockauf and L.W. Meyer, Effect of heat treatment conditions on the dynamic strength and failure behavior of titanium alloy Ti-6 Al-4V, *Journal De Physique. IV,* 2006, 134, 1091-1096.

[42] H. Fujii and H.G. Suzuki, Effect of cooling rates on microstructures of β treated α + β titanium alloys, *Journal of the Iron and Steel Institute of Japan,* 1991, 77, 1481-1488.

[43] W.D. Callister, Jr., *Materials Science and Engineering - An Introduction, 7th Edition,* John Wiley & Sons, Inc, 2007.

[44] X.J. Zhu, M.J. Tan and S. Thiruvarudchelvan, Effects of oxidization on the ductility of Ti-6A1-4V alloy during superplastic forming, *Materials Forum*, 2005, 29, 233-237.

[45] W.F. Hosford, *Mechanical Behavior of Materials*, 4th edition, Cambridge University Press, 1999.

[46] S.S.D. Rocha, G.L. Adabo, L.G. Vaz and G.E.P. Henriques, Effect of thermal treatments on tensile strength of commercially cast pure titanium and Ti-6Al-4V alloys, *Journal of Materials Science: Materials in Medicine,* 2005, 16, 759-766.

[47] J.D. Kwon, Y.T. Bae and S.J. Choi, The effect of microstructure on mechanical behaviour for titanium alloy (Ti-6Al-4V), *International Journal of Modern Physics B*, 2003, 17, 1297-1303.

[48] M. Jain, M.C. Chaturvedi, N.L. Richards and N.C. Goel, Strain rate sensitivity with forming characteristics of superplastic Ti-6Al-4V, *Materials Science and Engineering A*, 1991, 138, 205-211.

[49] A. El-Domiaty, The effect of strain, strain rate and temperature on formability of Ti-6Al-4V alloy, *Journal of materials processing technology,* 1992, 32(1-2), 243-251.

[50] C. Tang, J. Zhu, Y. Zhang and H. Zhou, Effect of strain rate ε on strain hardening exponent n of some metallic materials, *Acta Metall. Sinica (English Edition), Series B: Process Metallurgy & Miscellaneous*, 1994, 7, 183-186.

[51] N. Afrin, D.L. Chen, X. Cao and M. Jahazi, Strain hardening behavior of a friction stir welded magnesium alloy, *Scripta Materialia*, 2007, 57, 1004-1007.

[52] R. Markhandeya, S. Nagarjuna and D.V.V. Satyanarayana, Correlation of structure and flow behaviour of Cu-Ti-Cd alloys, *Materials Science and Engineering A,* 2006, 248, 233-243.

[53] K.V.U. Praveen, G.V.S. Sastry and V. Singh, Work hardening behavior of the Ni-Fe Based super alloy IN718, *The minerals, metals and materials society and ASM International,* 2008, 39, 65-78.

[54] G.E. Dieter, *Mechanical Metallurgy*, 3rd Edition, McGraw-Hill, 1986.

[55] X.Z. Lin and D.L. Chen, Strain hardening and strain-rate sensitivity of an extruded magnesium alloy, *Journal of Materials Engineering and Performance,* 2008, in print.

[56] U.S. Lindholm, Some experiments with the split Hopkinson pressure bar, *Journal of the mechanics and physics of solids,* 1964, 12, 317-335.

[57] Y.F. Shen, L. Lu, M. Dao and S. Suresh, Strain rate sensitivity of Cu with nanoscale twins, *Scripta Materialia*, 2006, 55, 319-322.

[58] R.K James, Fatigue behavior of solution-treated and quenched Ti-6Al-4V, *Materials Science and Engineering,* 1983, 57, 197-204.

[59] T.S. Srivatsan, W.O. Soboyejo and R.J. Lederich, Cyclic fatigue and fracture behavior of a titanium alloy metal matrix composite, *Engineering Fracture Mechanics,* 1995, 52(3), 467-491.

[60] S.Begum, D.L.Chen, S.Xu and A.A.Luo, Low cycle fatigue properties of an extruded AZ31 magnesium alloy, *International Journal of Fatigue,* 2008, in print, doi:10.1016/j.ijfatigue.2008.03.009.

[61] X.Z.Lin and D.L.Chen, Strain controlled cyclic deformation behavior of an extruded magnesium alloy, *Materials Science and Engineering A*, 2008, in print, doi:10.1016/j.msea.2008.05.016.

[62] G. Wang, L. Geng, D. Wang and S. Zhang, Low cycle fatigue of $(Al_2O_3+TiB_2+Al_3Ti)/Al$ composites fabricated by reactive hot pressing, *Fuhe Cailiao Xuebao/Acta Materiae Compositae Sinica*, 2004, 21(4), 118-123.

[63] L. Feng, W. Yue, C. Lihia, L. Zheng and Z. Jiyang, Low-cycle fatigue behavior of two magnesium alloys, *Journal of Materials Science,* 2005, 40, 529-1531.

[64] U. Noster and B. Scholtes, Isothermal strain-controlled quasi-static and cyclic deformation behavior of magnesium wrought alloy AZ31, *Zeitschrift fuer Metallkunde/Materials Research and Advanced Techniques,* 2003, 94(5), 559-563.

[65] D.E. Turner, Fatigue and Fracture Toughness Properties as a Function of Ti-6Al-4V ELI, *34th International SAMPE Symposium*, 1989, 290-299.

[66] D. Eylon and M. Pierce, Effect of microstructure on notch fatigue properties of Ti-6Al-4V, *Metallurgical transactions A,* 1976, 7A, 111-121.

[67] K. Shiozawa, S. Nishino and Y. Aikawa, Effect of microstructure on low-cycle fatigue behavior in Ti-6Al-4V alloy at elevated temperature, *Journal of the Society of Materials Science, Japan*, 1995, 44 (506), 1372-1377.

[68] B.B. Manderbrot, D.E. Passoja and A.J. Paullay, Fractal characteristics of fracture surfaces of metals, *Nature,* 1984, 308, 721-722.

[69] B.B. Manderbrot, Analysis and synthesis of fracture surface roughness related forms of complexity and disorder, *International Journal of Fracture,* 2006, 138, 13-17.

[70] J.J. Mecholsky Jr., Estimating theoretical strength of brittle materials using fractal geometry, *Materials Letters*, 2006, 60, 2485-2488.

[71] A. Carpinteri, A. Spagnoli and S. Vantadori, An approach to size effect in fatigue of metals using fractal theories, *Fatigue and Fracture of Engineering Materials and Structures*, 2002, 25(7), 619-627.

[72] R. Schiffmann, U. Wendt and W. Dahl, Damage mechanical investigations at ductile fracture of free-cutting steels by means of microscopy - void growth and fracture surface topography, *Journal De Physique IV*, 2001, 11(5), 5187-5193.

[73] A. Spagnoli, Fractality in the threshold condition of fatigue crack growth: An interpretation of the Kitagawa diagram, *Chaos, Solitons and Fractals*, 2004, 22(3), 589-598.

[74] J.J. Mecholsky Jr., J.K. West and D.E. Passoja, Fractal dimension as a characterization of free volume created during fracture in brittle materials, *Philosophical Magazine A*, 2002, 82(17-18), 3163-3176.

[75] O.A. Hilders, L. Sáenz, M. Ramos, and N.D. Peña, Effect of 475°C embrittlement on fractal behavior and tensile properties of a duplex stainless steel, *Journal of Materials Engineering and Performance*, 1999, 8, 87-90.

[76] O.A. Hilders, M. Ramos, N.D. Pena and L. Saenz, Fractal geometry of fracture surfaces of a duplex stainless steel, *Journal of Materials Science*, 2006, 41(17), 5739-5742.

[77] L.H. Dai and G.Z. Wu, Relation between fracture toughness and fractal dimension of fracture surface for PP/AT composites, *Acta Materiae Compositae Sinica*, 1996, 13(4), 70-74.

[78] J.C. Hsiung and Y.T. Chou, Fractal characterization of fractal surface of high strength low alloy steel, *Journal of material science,* 1998, 33, 2949-2953.

[79] Z.G. Wang, D.L. Chen, X.X. Jiang, S.H. Ai and C.H. Shih, Relationship between fractal dimension and fatigue threshold value in dual-phase steels, *Scripta Metallurgica*, 1988, 22, 827-832.

[80] M.A. Issa, M.S. Islam and A. Chudnovsky, Fractal dimension-a measure of fracture roughness and toughness of concrete, *Engineering Fracture Mechanics*, 2003, 70(1), 125-137.

[81] L. E. Richards and B. D. Dempsey, Fractal characterization of fractured surfaces in Ti-4.5 Al-5.0 Mo-1.5 Cr (corona 5), *Scripta Metallurgica*, 1988, 22, 687-689.

[82] C. S. Pande, L. E. Richards, N. Louat, B. D. Dempsey and A. J. Schwoeble, Fractal characterization of fractured surfaces, *Acta Metall.*, 1987, 35(7), 1633-1637.

[83] T. V. Vorburger, H.G. Rhee, T. B. Renegar, J.F. Song and A. Zheng, Comparison of optical and stylus methods for measurement of surface texture , *The International Journal of Advanced Manufacturing Technology*, 2007, 33, 110-118.

[84] A. Mannelqvist and M.R. Groth, Comparison of fractal analyses methods and fractal dimension for pre-treated stainless steel surfaces and the correlation to adhesive joint strength, *Applied Physics A: Materials Science and Processing,* 2001, 73, 347.

[85] J.Y. Go and S.I. Pyun, Fractal approach to rough surfaces and interfaces in electro chemistry, *Modern aspects of Electro Chemistry, Number 39*, edited by C. Vayenas *et al.*, Springer, New York, 2005, 167-229.

[86] W. Drury and A.M. Gokhale, Measurement and interpretation of fracture surface fractal dimension, *ASTM Special Technical Publication No.1165,* 1993, 295-310.

[87] E. Charkaluk, M. Bigerelle and A. Iost, Fractals and fracture, *Engineering Fracture Mechanics*, 1998, 61, 119-139.

[88] A.L. Horovistiz and L.R.O. Hein, Fractal analysis along stretch zone for an aluminum alloy, *Materials Letters,* 2005, 59, 790-794.

[89] P. Kotowski, Fractal dimension of metallic fracture surface, *International Journal of Fracture*, 2006, 141, 269.

[90] M. Bigerelle and A. Iost, Statistical artefacts in the determination of the fractal dimension by the slit island method, *Engineering Fracture Mechanics*, 2004, 71, 1081-1105.

[91] X.W. Li, J.F. Tian, S.X. Li and Z.G. Wang, Application of a fractal method to quantitatively describe some typical fracture surfaces, *Materials Transactions*, 2001, 42(1), 128-131.

[92] N.Afrin, D.L.Chen, X.Cao and M.Jahazi, Microstructure and tensile properties of friction stir welded AZ31B magnesium alloy, *Materials Science and Engineering A*, 2008, 472(1-2), 179-186.

[93] P. Zhu and B.S. Chen, 3D topography of fractured surfaces and mechanical properties under instrumented impact loading, *Acta Metallurgica Sinica,* 1998, 34(1), 63-69.

[94] M. Tanaka, Y. Kimura, N. Oyama and R. Kato, Relations between the creep-rupture properties and the fractal dimension of three-dimensional fracture surface in a cobalt base alloy, *Journal of Materials Science*, 2006, 41, 6181-6184.

[95] Y. Kimura, J. Taguchi, M. Tanaka, L. Chouanine and R. Kato, Quantitative analysis of three dimensional fatigue fracture surface reconstructed by stereo matching method, *ISIJ international*, 2003, 43, 1453-1460.

[96] H.W. Zhou and H. Xie, Direct estimation of the fractal dimensions of a fracture surface of rock, *Surface Review and Letters*, 2003, 10, 751-762.

[97] ANSI/ASME B46.1-2002, Surface Texture (Surface Roughness, Waviness and Lay), *American Society of Mechanical Engineers*, 2002.

[98] O.A. Hilders, N.D. Pena and O.A. Roa, Model to predict the fractal dimension of fractured surfaces of 7075 aluminium alloys based on Koch's fractal curve and mechanical properties, *Materials Science Forum*, 1996, 217-222(3), 1485-1490.

[99] Y.T. Lee, M. Peters and G. Welsch, Elastic moduli and tensile and physical properties of heat treated and quenched powder metallurgical Ti-6Al-4V alloy, *Metallurgical Transactions A*, 1991, 22, 709-714.

BALAJI DEVATHA VENKATESH

EDUCATION

Master of Applied Science (Aug 2008)
Ryerson University, Toronto, ON
Major: Mechanical Engineering
Bachelor of Engineering (Aug 1999)
Sir M. Visvesvaraya Institute of Technology, Bangalore, India
Major: Mechanical Engineering

EXPERIENCE

Teaching Assistant, Sep 2006- Aug 2008
Ryerson University, Toronto, ON, Canada

Design Engineer, Dec 2003- Aug 2006
General Motors Technical Center India, Bangalore, India

Tool Design Engineer, Apr 2000 – Dec 2003
Aerospace division, Hindustan Aeronautics Limited, Bangalore, India

LIST OF PUBLICATIONS (over the past two years during my MASc study)

A. Refereed journal papers (published or under review):

1. B.Venkatesh, D.L.Chen and S.D.Bhole, Three-dimensional fractal analysis of fracture surfaces in a titanium alloy for biomedical applications, ***Scripta Materialia***, 2008, 59(4), 391-394.

2. B.D.Venkatesh, D.L.Chen and S.D.Bhole, Effect of heat treatment on mechanical properties of Ti-6Al-4V ELI alloy, submitted to ***Materials Science and Engineering A***, 2008 (under review).

3. B.D.Venkatesh, D.L.Chen and S.D.Bhole, Tensile and cyclic deformation characteristics of a titanium alloy for biomedical applications, a journal manuscript to be submitted (*under revision after Dr. Chen's first review*).

B. Conference presentations:

1. B.Venkatesh, D.L.Chen and S.D.Bhole, Strain hardening and strain-rate sensitivity of extra-low interstitial grade Ti-6Al-4V alloy, the 20th Canadian Materials Science Conference (CMSC), Edmonton, Alberta, edited by R. Eadie and T. Etsell, Met Soc, June 16-19, 2008, p.2. (oral presentation given by B.Venkatesh).

2. B.Venkatesh, D.L.Chen and S.D.Bhole, Effect of thermal oxide hardened layer on mechanical properties of Ti-6Al-4V ELI alloy, Abstracts Book, MRS International Materials Research Conference, Chongqing, China, June 9-12, 2008, pp.355-356 (oral presentation given by Dr. Chen).